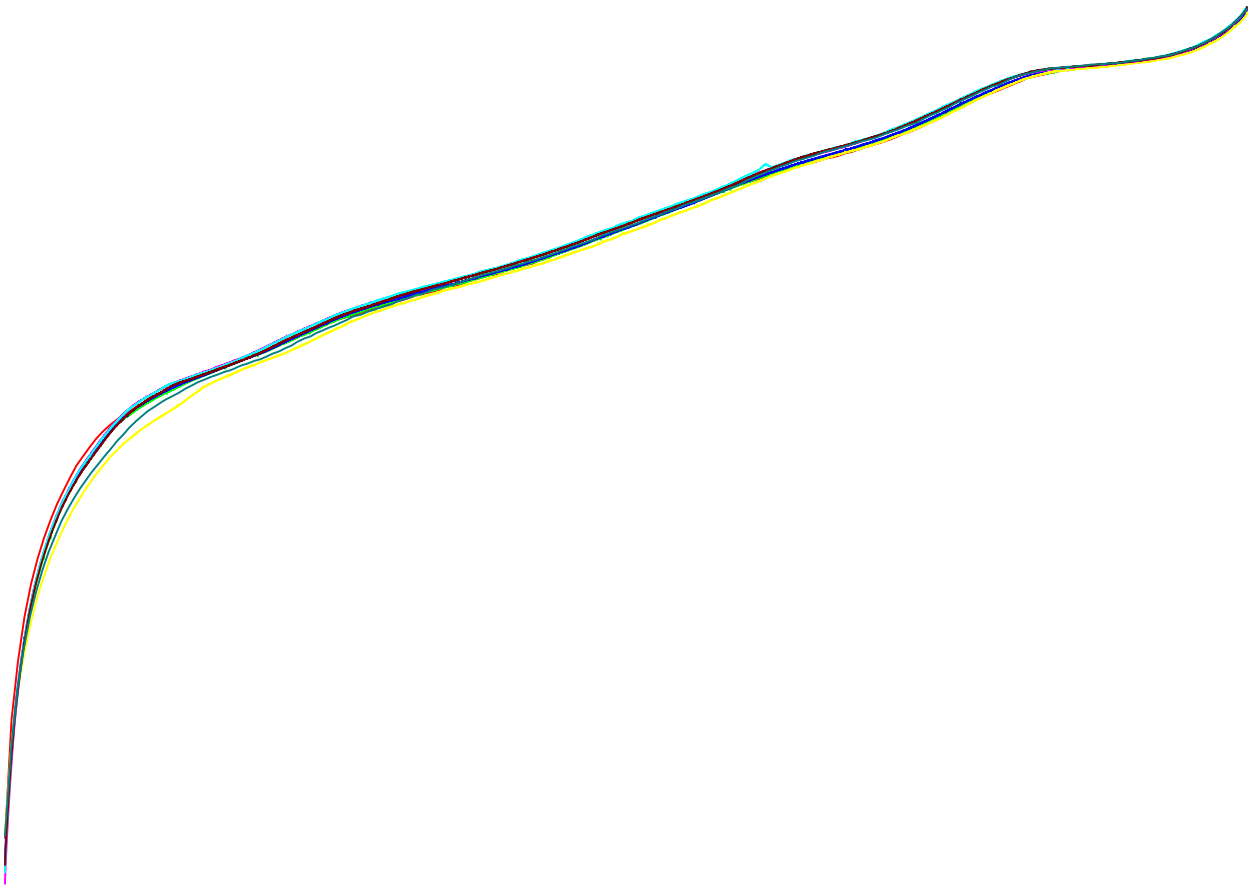

Parametrization of Lithium-Ion Battery Cell Model and Test Rig Development for BMS Application

MPSYS & MPMOB

Victor Dolk & Pontus Rhedin

ELECTRICAL DEPARTMENT

CHALMERS UNIVERSITY OF TECHNOLOGY
Gothenburg, Sweden 2024
www.chalmers.se

Master's thesis 2024

Parametrization of Lithium-Ion Battery Cell Model and Test Rig Development for BMS Application

VICTOR DOLK
PONTUS REHDIN

CHALMERS
UNIVERSITY OF TECHNOLOGY

Department of Energy and Environment
Division of electric power engineering
Examiner: Stefan Lundberg
T-engineering supervisors: Fredrik Assarsson, Henrik Glad, Leif Hermansson & Olof Martander
Chalmers University of Technology
Gothenburg, Sweden 2024

Parametrization of Lithium-Ion Battery Cell Model and Test Rig Development for BMS Application

VICTOR DOLK & PONTUS RHEDIN

Supervisor: Fredrik Assarsson, Henrik Glad, Leif Hermansson & Olof Martander, T-engineering
Examiner: Stefan Lundberg, Department of Energy and Environment

Master's Thesis 2024
Department of Energy and Environment
Division of electric power engineering
Chalmers University of Technology
SE-412 96 Gothenburg
Telephone +46 31 772 1000

Cover: Open circuit voltage for eight different temperatures of a lithium ion battery cell.

Typeset in LaTeX
Printed by Chalmers Reproservice
Gothenburg, Sweden 2024

Abstract

The rising demand for electric vehicles has driven significant advancements in lithium ion battery technology. A critical function of the Battery Management System (BMS), central to electric vehicle performance, is the estimation of the State of Charge (SOC). Kalman filtering is a widely used method for SOC estimation. Additionally, estimating battery degradation over time, known as the State of Health (SOH), is vital for understanding how the battery will age. Another important aspect of the BMS is to estimate the State of Power (SOP) to limit the battery's allowable currents to prevent damage. Developing an accurate battery model requires measurement data from a real battery cell, and since lithium ion battery cells are temperature dependent, these measurements must be conducted across a wide range of temperatures to capture this dependency. This thesis focuses on the development of a measurement rig, enabling the collection of data necessary for the parameterization of the battery model. This model is then used to estimate SOC, SOH, and SOP. This is conducted for two different lithium ion cells with the same cell chemistry.

The simulation results show that the dual Resistance Capacitance (RC) Thévenin Equivalent Circuit Model (ECM) with thermal dependency is beneficial due to the trade off between low model complexity and high accuracy. The parameters used for the model were based on multiple measurements conducted for eight different temperatures. The measurement methods were chosen and evaluated with time efficiency and high accuracy in mind. The parameters were obtained by using different curve fitting methods with respect to open circuit voltage OCV, SOC and temperature. The terminal voltage measurement from the measurement equipment was used to verify model and parameterization accuracy where the mean modeling error for the blue cell is 0.1050% while median error for the grey cell is 0.1317%. Both simulation and parameterization output were satisfactory.

The SOC results on real data sets show that Kalman filtering is a robust and beneficial method since the estimated SOC for both filters were within the 3% SOC error bounds. The Unscented Kalman Filter (UKF) performs better in the presence of high uncertainties and nonlinearities compared to the extended Kalman filter (EKF). However, both filters performed similarly due to easy nonlinearities and common nominal conditions. Therefore the operating conditions will decide which estimation algorithm to be used. The implemented SOP algorithm estimates the maximum and minimum current to be drawn at every time instance with respect to SOC and voltage limits. The algorithm also provides highly accurate power estimations for 5, 10, and 30 seconds into the future. The implemented SOH algorithm based on cycling measurement shows a clear degeneration trend for both parameters it has been based on. The SOH estimation is a function of changes in OCV and capacity with respect to a number of cycles.

Keywords: Battery, Lithium, ECM, SOC, SOH, Estimation, SOP, Kalman, Measurement, Simulation, UKF, EKF.

Acknowledgements

We would like to express our gratitude to our examiner, Stefan Lundberg, for the feedback and support throughout the this thesis. His expertise has been invaluable in guiding this research.

We are also grateful to our four supervisors at T-engineering, Fredrik Assarsson, Henrik Glad, Leif Hermansson & Olof Martander. Their combined support and mentorship have been crucial to our success. Thank you all for your invaluable contributions and for the opportunity to write this thesis at your company.

Victor Dolk & Pontus Rhedin, Trollhättan, June 2024

Contents

List of Figures

List of Tables

1
Introduction

1.1 Background

In response to the urgent need to mitigate climate change, the automotive industry is increasingly turning to electric vehicles as a solution to reduce carbon emissions [1]. Electric vehicles offer several advantages, including decreased emissions, energy efficiency, and reduced noise pollution [2]. To power the electric vehicles lithium ion batteries are commonly used. These batteries consist of numerous single cells connected in series and parallel to meet the high energy and power demands of electric vehicles [3]. Despite having similar specifications, variations in manufacturing conditions lead to differences in the characteristics of individual cells, which tend to increase with usage [4]. Moreover, the strict operational restrictions based on voltage, temperature, and current add complexity to battery management. To address these challenges, a Battery Management System (BMS) is crucial. Among its key functions,State of Charge (SOC), State of Health (SOH) and State of Power (SOP) estimation is paramount [5]. As SOC cannot be directly measured, SOC estimation relies on factors such as the concentration of lithium ions at the electrodes [6]. However, due to differences among cells, accurately determining SOC for an entire battery pack proves challenging. Various factors contribute to the complexity of reliable SOC estimation, including noisy sensor measurements, temperature and parameter variations, battery aging, and the nonlinear behavior of batteries [7].

Given the substantial expense associated with battery cells, the implementation of an effective BMS stands as a crucial cost saving measure for companies. Beyond the immediate production phase, a robust BMS plays a vital role in prolonging the lifespan of battery cells [8]. A well engineered BMS not only safeguards battery health but also ensures slow degradation. By harnessing the full potential of the batteries in electric vehicles customers can extract maximum value from their investment. In essence, the integration of an efficient BMS not only drives down production costs but also promotes a more sustainable and rewarding ownership experience for consumers.

In this thesis, different methods of Kalman filtering will be employed to accurately and reliably estimate SOC. SOH will be estimated using measurement data from the cycling of batteries. SOP estimations will be done to estimate current and future power outputs. The project will focus on the development of a comprehensive lithium ion battery cell model. A measurement campaign will include two types of

lithium ion cells. The data will be used to parameterize the model. A test rig capable of measuring the cells accurately at different temperatures will also be examined.

1.2 Aim

To measure the parameters of two different cells and from these measurements build a model for the cell valid for different SOC and temperatures. Based on the model investigate different estimation methods for SOC together with at least one method for SOH and SOP estimation and to evaluate these methods.

1.3 Objectives

- What tests and methods can be employed to rapidly and effectively ascertain the essential parameters required for developing a reliable battery cell model, with a focus on ensuring both accuracy and time savings?
- What parameters are necessary to develop an effective battery cell model for BMS, and how can these parameters be identified in a manner that is both accurate and time effective?

2

Behavior and modeling of lithium ion cells

2.1 Overview of lithium ion batteries

Lithium ion batteries for vehicle applications usually consist of multiple series and parallel connections of lithium ion cells. Lithium ion cells is an electrochemical battery that is rechargeable and therefore allows lithium ions to move back and forth between solid materials that conduct electricity [9]. The ion's are transformed into electrical energy whenever an external load is connected to the battery poles. The difference in electric potential between the poles results in a terminal voltage V_t $[V]$. Different types of batteries are designed for specific purposes and therefore have different types of chemical compositions. The different chemical compositions results in varying terminal voltages. The benefits of the lithium ion chemistry compared to other types of cell chemistry's are the total storage energy capability compared to its weight and volume, which is a crucial factor for vehicle applications. Figure 2.1 [10] shows that lithium ion cells have a relatively high energy storage capability compared to its weight and volume, compared with other chemistries. The lithium ion cell chemistry used in this thesis consists of two different types of lithium nickel manganese cobalt oxide (Li-NiMnCoO2) cells which are designed and manufactured by two different companies.

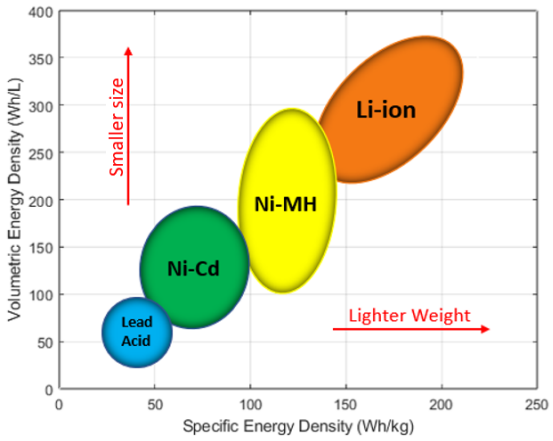

Figure 2.1: Volumetric energy density vs specific energy density [10].

The battery cells generally consist of the following different parts: cathode, anode, electrolyte, current collectors and separator. During discharge, when a current is drawn from the cell, the anode (negative electrode) undergoes a chemical oxidation which results in a release of lithium ions and electrons which can be seen in Figure 2.2 reproduced from [11] under the CC BY-NC-SA 2.0 DEED license.

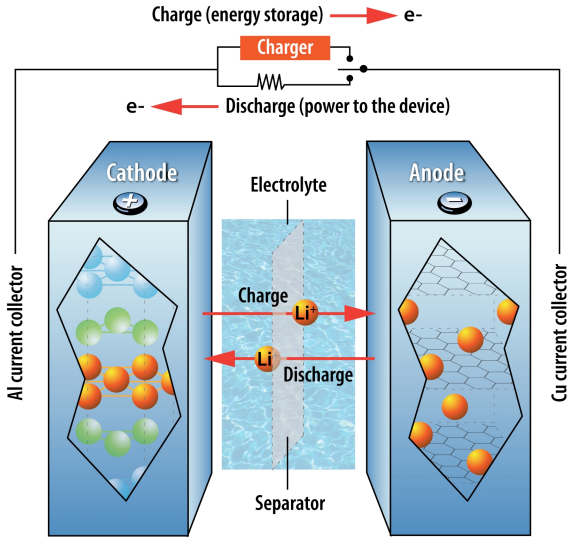

Figure 2.2: Battery cell during discharge. Reproduced from [11] under the CC BY-NC-SA 2.0 DEED license.

The ions move through the electrolyte and perform a mass transport through the separator and finally defuses on to the cathode (positive electrode) [12]. The separator prevents short circuits from occurring. The released electrons are not able to do the mass transport and therefore will flow to the current collector placed on the battery terminal to which the external load is attached, resulting in a current flow. The charging procedure is the same process but reversed. The chemical oxidation is happening at the cathode, and the anode will be the receiver of electrons and mass transport of ions. The capacity of the cell, measured in Ampere-hours (Ah), is determined by the total number of lithium particles that can be stored within the spaces between the two electrodes [9], [12]. The current is defined as positive when the battery is discharged and negative when the battery is charging.

2.1.1 State of charge

State of Charge (SOC) defines the amount of charge stored within one or multiple cells connected. The SOC function is defined as

$$\mathrm{SOC}(t) = \frac{Q(t)}{Q} \cdot 100[\%] \tag{2.1}$$

where $Q(t)$ $[Ah]$ defines the available charge and Q $[Ah]$ is defined as the nominal capacity [13]. A battery with full charge capacity has a SOC of 100% while a fully discharge battery has a SOC level of 0%. SOC is a key parameter for BMS systems and is used when controlling the electrical vehicle. There are multiple short and

long term factors affecting the SOC such as the size of the current drawn from the cell during discharge or the size of the current that have been used during charge. The cell temperature during charge and discharge also affects the SOC [13].

2.1.2 Open circuit voltage

Open Circuit Voltage (OCV) is defined as the no load voltage across the battery terminals when the battery has been held at rest for a period of time and no current is flowing through it. The OCV serves as an indicator of the electric potential or energy state of the battery within a specific energy storage point and therefore provides information about the available voltage from the battery cell [12], [14]. The voltage reflects the chemical potential difference between the battery's electrodes and is therefore affected by terms of SOC and temperature. These terms are time varying which directly increases the complexity of OCV. OCV is a nonlinear function of SOC described as:

$$OCV(t) = f(SOC) \tag{2.2}$$

OCV is often modeled as a multi polynomial function or mapped into a lookup table from cell measurements [14]. An example of OCV-SOC characteristics of an lithium ion cell can be seen in Figure 2.3.

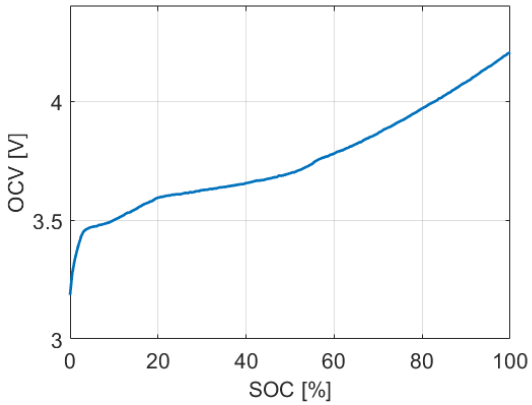

Figure 2.3: OCV-SOC voltage profile of a lithium-ion battery.

Depending on the cell chemistry, a lithium ion battery cell usually has to a certain degree linear behavior between 10% and 90% SOC. Due to its flatness a small deviation in OCV would correspond to a large variation in SOC [12]. This implies that small measurement disturbances such as noise might have a substantial impact on SOC estimation. Thereby a precise and accurate voltage measurement with low noise impact is crucial to gather data that is useful for creating the OCV-SOC function described in (2.2) [12].

2.1.3 Polarization voltage

The polarization voltage is the difference between the cell's internal voltage and the measured terminal voltage. This difference comprises various components, categorized as concentration polarization, activation polarization and ohmic losses. Concentration polarization occurs due to non-homogeneity at the surface where reactions take place. This results in localized regions where reactants do not reach the reaction surface quickly enough to maintain stable reactant concentrations, especially at high current densities. The current density at which this phenomenon causes a drop in cell potential is called the limiting current. Concentration polarization can occur at both the anode and cathode [15].

Activation polarization occurs due to the voltage difference required between the anode and cathode to sustain electrochemical reactions. It can be viewed as a voltage threshold that must be surpassed to initiate current flow from the battery. Activation polarization is often considered relatively independent of current density, but its behavior can vary depending on factors such as operating conditions and materials used in the battery [15].

Ohmic losses in a battery are attributed to the resistance within its internal components, such as the electrodes and electrolytes. These losses arise due to the conversion of electrical energy into heat as current flows through the conductive pathways within the battery. Ohmic losses will lead to a drop in voltage across the battery terminals and contribute to overall inefficiencies in energy conversion [15].

2.1.4 Hysteresis

Hysteresis is a phenomenon that appears as a difference in OCV. This means that the OCV value differs between charge and discharge for the same SOC value at a given temperature [14]. The voltage hysteresis has a clockwise oriented graph, resulting in discharge OCV being lower than charge OCV. The hysterics also have a major and minor loop behavior meaning that the OCV will have different hysteresis behavior depending on where in the span of 0% to 100% SOC [16]. The major loop is defined as the hysteresis curvature the OCV voltage has during charge and discharge between 0% to 100% and 100% to 0%. However, if the battery cell is partially discharged or charged from a SOC value different than 100% or 0%, the curvature will not follow the same path as for the major loop and instead end up in a smaller minor loop. One way to model this is either with a self correcting electric Equivalent Circuit Model (ECM) or taking the average OCV value between charge and discharge [16]. In Figure 2.4 the battery impedance and hysteresis effect are displayed.

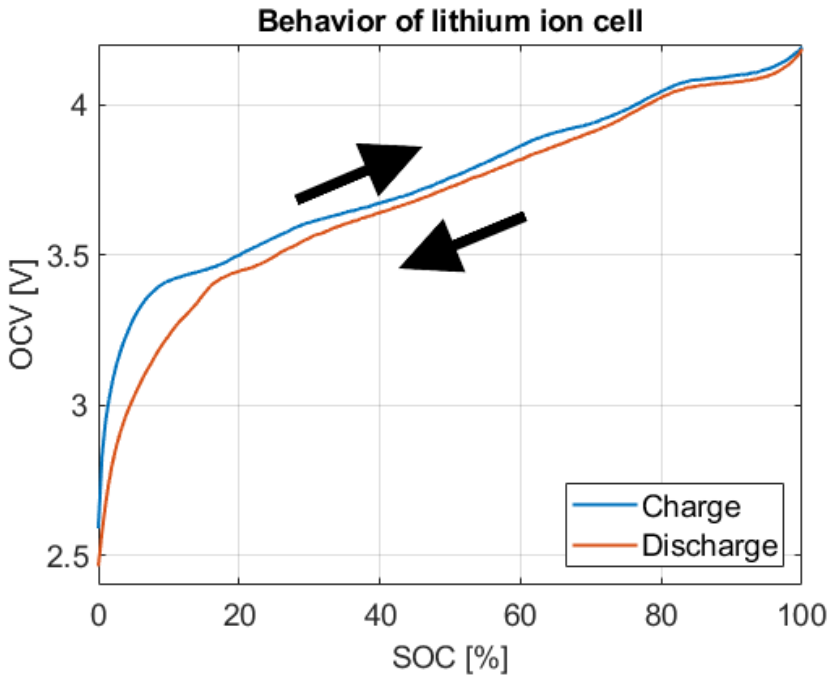

Figure 2.4: OCV-SOC lithium-ion battery voltage characteristics.

This results in two different OCV-SOC voltage curvatures between the charge and discharge of the cell.

2.1.5 State of health

State of health (SOH) is an indication parameter that indicates how much of the remaining total capacity is left compared to the cell capacity at the beginning of life. During usage and cycling of the battery cell, the total capacity will decrease until the battery cell no longer can fulfill the rated performance it had at the beginning of life [17]. When a lithium ion battery has degraded to 80% of its nominal capacity, it is deemed to have reached its end of life. SOH is defined as

$$\text{SOH}(t) = \frac{Q_{max}(t)}{Q_{max,rated}} \cdot 100[\%] \tag{2.3}$$

where $Q_{max}(t)$ $[C]$ is the actual charge capability and $Q_{max,rated}$ $[C]$ is the rated charge capability. SOH can also be defined as a function of changes in OCV as

$$\text{SOH}(t) = \frac{OCV(t)}{OCV_{rated}} \cdot 100[\%] \tag{2.4}$$

where OCV_{rated} $[V]$ is the rated maximum voltage from factory and $OCV_(t)$ $[V]$ is the OCV measured after the cell has been charged up to OCV_{rated}, and then relaxed for one hour. The aging mechanism is affected by a number of driving cycles, the temperature at charge and discharge, battery cell design and usage which makes the aging process of a battery complex [17].

2.1.6 State of power

State of Power (SOP) provides the instantaneous power capability of the lithium ion cell without violating preset operational design limits such as V_{max}, V_{min}, $I_{max,charge}$ and $I_{max,discharge}$ provided by the cell manufacturer. This measurement is specified separately for charging and discharging, as the power capabilities may differ between the two processes. SOP is a varying parameter that is dependent on cell chemistry, internal cell impedance, SOC, cell temperature, degradation and maximum charge/discharge rates. By monitoring SOP, batteries can be optimized for performance and safety [18]. SOP for charge and discharge can be calculated as

$$SOP_c(t) = \frac{P_{max,charge}(t)}{P_{maxn,charge}} \cdot 100[\%] \tag{2.5}$$

$$SOP_d(t) = \frac{P_{max,discharge}(t)}{P_{maxn,discharge}} \cdot 100[\%] \tag{2.6}$$

where $P_{maxn,x}$ $[W]$ is the maximum rated power of the battery for charge respectively discharge and $P_{max,x}(t)$ $[W]$ is the actual maximum charge power that can be drawn from the battery with respect to SOC, current, temperature and maximum and minimum voltage levels. This indicator is crucial for maintaining optimal power levels during charging or discharging, thereby extending battery lifespan. Additionally, it aids in defining conditions for significant charges or discharges in peak power applications [19].

2.2 Models for battery cells

the battery model can take different forms, but the most commonly used is an ECM, which aims to represent the dynamics of a battery as accurately as possible [20]. Equivalent Circuit Modeling (ECM) is a modeling method that tries to capture the battery dynamics with pure electrical behavior such as currents, voltages, capacitors and resistances. Using the physical theory of electric circuits, it is possible to derive systems of Ordinary Differential Equations (ODEs) for low-dimensional systems [21]. These systems are generally nonlinear due to the dependency of SOC and temperature. These types of models are able to capture most of the essential electrical phenomena caused by the battery during charge and discharge with good accuracy. Because of the physical ODE equations, the ECM is easily executable in real time, which is advantageous for BMS systems. ECM is often modeled as Thévenin circuits with one voltage source capturing the OCV, one series resistance representing the ohmic resistance of the cell and multiple RC parallel connection links which capture the time constants of the system. There is a design trade off between the number of RC links which implies system complexity and model accuracy [21].

Black box modeling is an approach where the focus is on observing the input-output relationship of a system rather than focusing on its internal mechanisms. Machine learning algorithms like neural networks are trained to map inputs to outputs, with

the internal processes remaining opaque or "black" to the observer, who concentrates solely on the efficacy of the mapping. While this methodology could indeed be applied to model a lithium ion battery, it suffers from the disadvantage of high computational costs, making it unsuitable for implementation within a BMS [22].

Electrochemical modeling refers to a method where mathematical models of the chemical reactions occurring inside a battery are modeled. These mathematical models consist of equations that describe the transport of ions and electrons within the battery electrodes and electrolyte, as well as the kinetics of the electrode reactions. By simulating the electrochemical processes, such models can predict the battery's behavior under different operating conditions very accurately [23]. While electrochemical modeling provides a comprehensive understanding of the processes within the battery, its major drawback lies in its substantial computational cost, rendering it unsuitable for implementation within a BMS.

2.2.1 Measurement techniques of batteries

Electrochemical Impedance Spectroscopy (EIS) is a precise electrochemical technique used for its ability to measure intricate electrochemical processes within complex systems, such as batteries [24]. Measurements can be conducted in two different ways. The first method, known as galvanostatic control, is a method where Alternating Current (AC) is applied and the AC voltage response is measured. The other one is called potentiostatic control and is the opposite of galvanostatic control [25]. Therefore the battery is not charged or discharged during measurement which means that the integrity of the battery is preserved. One of the significant benefits of EIS is its high accuracy, which provides detailed data for analysis [26]. However, a notable disadvantage is the challenge of fitting EIS data to a specific battery model. Therefore, the battery model may be chosen to fit the data, rather than the other way around. This becomes problematic as the choice of battery model influences different estimation methods. Since the battery model might change depending on the battery, adapting the estimation methods can be time consuming and may require significant adjustments.

Another measurement technique used to parameterize batteries is Direct Current (DC) pulses. Using this method, the battery undergoes numerous DC pulse cycles, containing both charge and discharge cycles, to evaluate its properties and behavior. A typical cycle begins with draining the battery from 100% SOC to 10% SOC, with each pulse representing a 10% decrease in SOC. To capture relaxation effects, the next pulse is applied when the battery is close to stable OCV. The battery is then discharge until it reaches 0% SOC, and then charged incrementally with 10% charge pulses until it reaches 90% [27]. The final 10% in the ends cannot be parameterized using a 10% pulse as it would potentially could exceed maximum voltage when charging and minimum voltage when discharging. This depends on how the internal resistance changes and the temperature dependency of the battery cell. A typical DC pulse can be seen in Figure 2.5.

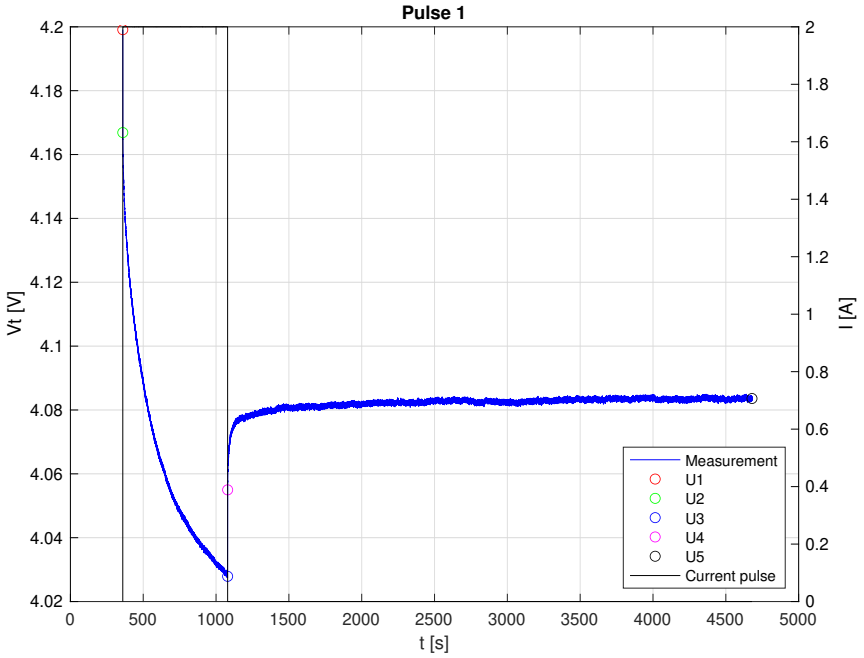

Figure 2.5: DC pulse response for a typical lithium ion battery.

The pulse can be divided into different regions where U1 to U5 represents different parts. U1 to U2 and U3 to U4 can be represented as a resistive drop while U2 to U3 and U4 to U5 can be seen as time constants. This process effectively captures the charge and discharge characteristics of the battery for a specific ambient temperature. To explore the influence of temperature on the battery, these measurements are repeated at various ambient temperatures. Since DC pulses directly affect the integrity of the battery, these measurements can be utilized to cycle through the battery multiple times, enabling the capture of degradation effects [27]. To capture both degradation and temperature effects, a measurement campaign for a single battery can be very time consuming.

2.2.2 Parameter identification

There are generally two different methods for determining the parameters from measurement data. The first one is the online parameter identification method, which is based on a battery model that utilizes different types of estimators to estimate the model parameters in real time. The estimation is usually done with either Recursive Least Square (RLS) or Kalman filter estimation [28]. The benefit of the online method is that the battery parameters are time-varying, which to a large extent can be solved by the two different methods. This also implies that these methods are computationally demanding and easily affected by initial parameters, such as initial guess in the Kalman filter and the forgetting factor within the RLS algorithm [28], [29].

The offline method is based on a large set of multiple charge and discharge measurement data. These sets of data are then used to extract the parameters from the experimental data into look up tables using curve fitting techniques [29]. This method

is dependent on having multiple measurements on the cell and small changes in temperature between the measurements to have a high resolution model with small errors. The offline method is also limited when it comes to unexpected behavior since the model will be running on pre-measured values even though the parameters are time dependent [29].

2.3 SOC estimation

Unlike the fuel tank in an Internal Combustion Engine (ICE) vehicle, where the fuel level can be directly measured, the charge of a battery cannot be directly measured [6]. Therefore, several different estimation methods have been developed in order to handle this problem. With the rise of electric vehicles in the past years and the high cost of lithium ion batteries, the focus on estimating the batteries properties correctly has intensified. Several different SOC estimation methods have been developed in order to handle this problem. Early estimation methods include current based methods, also called Coulomb Counting (CC). This method CC is a physical approach that estimates the SOC via current measurements. The change in charge (Q) is dependent on the amount of current (I) which has passed through the battery cell resulting in $\dot{Q}(t) = I(t)$ [30]. By applying this, the CC estimation of SOC can be determined from (2.1) as:

$$S\dot{O}C(t) = -\frac{\eta}{Q}I(t) \quad \Rightarrow \quad SOC(t) = SOC(0) - \frac{\eta}{Q}\int_0^t I(t) \tag{2.7}$$

where η [%] is defined as the Coulombic efficiency and $SOC(0)$ [%] is the initial SOC. The current is defined as positive during discharge and negative during charge. While this SOC method is computationally efficient, its flaw lies in that it is easily affected by measurement noise and bias, resulting in that the SOC is prone to drift over time [31],[30]. To handle this, more advanced estimation algorithms such as the Kalman filter are introduced. The Kalman filter is an estimation algorithm that utilizes probability theory, specifically Bayesian inference, to iteratively estimate the states of a dynamic system based on current, voltage and temperature measurements. Since a battery behaves highly nonlinear, the Extended Kalman filter (EKF) and Unscented Kalman filter (UKF) are usually applied [32]. These methods have been proven to work very well, outperforming the CC method.

2.3.1 Extended Kalman filter algorithm

The EKF is an advanced adaptation of the classic Kalman filter, specifically designed to address the challenges posed by nonlinear systems and non Gaussian noise distributions [12]. The EKF operates through a two step process, the prediction step and the update step. During the prediction step, the EKF estimates system states forward in time using a state transition model coupled with an associated process noise model. This step estimates the future state based on the system's dynamics while accounting for uncertainties introduced by the system's processes. Next, in the update step, noisy measured data is assimilated to refine the state estimate and mitigate uncertainty. Here, the EKF compares predicted measurements generated

by the system model with actual measurements collected from sensors, adjusting the state estimate accordingly. A distinctive feature of the EKF lies in its approach to handling nonlinearities within the system model. Through the utilization of a first order Taylor series expansion, the system model is linearized at the current estimate point. This enables the EKF to effectively approximate the nonlinear system dynamics, making it useful in estimating system states for nonlinear systems. Therefore, the EKF has been proven to accurately estimate SOC for batteries [33]. The EKF is defined as [12]

$$\hat{x}_{k|k-1} = f(\hat{x}_{k-1|k-1}, u_k) \tag{2.8}$$

where $\hat{x}_{k|k-1}$ is the predicted state estimate at time k given measurements up to time $k-1$, $\hat{x}_{k-1|k-1}$ is the previous state estimate at time $k-1$ and u_k is the control input at time k. Next, the prediction of the error covariance matrix is calculated using the state transition matrix F_k, which accounts for how uncertainties propagate through the system dynamics, and the process noise covariance Q_k

$$P_{k|k-1} = F_k P_{k-1|k-1} F_k^T + Q_k \tag{2.9}$$

where $P_{k|k-1}$ is the predicted error covariance at time k, F_k is the state transition matrix at time k and Q_k is the process noise covariance at time k. This equation predicts how the uncertainty in the state estimate evolves over time, accounting for both the uncertainty in the previous estimate $P_{k-1|k-1}$ and the process noise. Moving to the update step, the first task is to predict the measurement using the predicted state estimate

$$\hat{z}_k = h(\hat{x}_{k|k-1}) \tag{2.10}$$

where $\hat{z}_k$ is the predicted measurement at time k and $h(\cdot)$ is the measurement function. With the predicted measurement in hand, the innovation or measurement residual y_k is computed as the difference between the actual measurement z_k and the predicted measurement $\hat{z}_k$

$$y_k = z_k - \hat{z}_k \tag{2.11}$$

where z_k is the actual measurement at time k, y_k is the innovation or measurement residual at time k. Next, the measurement prediction covariance S_k is updated to incorporate both the uncertainty in the predicted measurement and the measurement noise covariance R_k

$$S_k = H_k P_{k|k-1} H_k^T + R_k \tag{2.12}$$

where S_k is the innovation covariance at time k, H_k is the measurement Jacobian matrix at time k and R_k is the measurement noise covariance at time k. The matrix H_k is the Jacobian matrix of the measurement function evaluated at the predicted state $\hat{x}_{k|k-1}$. It describes how small changes in the state affect the predicted measurement. Now, the Kalman gain K_k is calculated, which determines the weighting between the predicted state estimate and the measurement update

$$K_k = P_{k|k-1} H_k^T S_k^{-1} \tag{2.13}$$

where K_k is the Kalman gain at time k. A higher Kalman gain gives more weight to the measurement update, while a lower Kalman gain gives more weight to the predicted state estimate. With the Kalman gain computed, the updated state estimate $\hat{x}_{k|k}$ is obtained by combining the predicted state estimate with the measurement update

$$\hat{x}_{k|k} = \hat{x}_{k|k-1} + K_k y_k \tag{2.14}$$

where $\hat{x}_{k|k}$ is the updated state estimate at time k. This equation adjusts the predicted state estimate based on the innovation y_k weighted by the Kalman gain. Finally, the error covariance matrix $P_{k|k}$ is updated to reflect the reduced uncertainty in the state estimate after incorporating the measurement

$$P_{k|k} = (I - K_k H_k) P_{k|k-1} \tag{2.15}$$

where I is the identity matrix. This equation adjusts the error covariance matrix based on the Kalman gain and the Jacobian matrix, ensuring that the uncertainty in the state estimate is appropriately updated. These steps together form the core of the EKF, allowing it to effectively estimate the state of nonlinear systems by iteratively predicting, updating, and refining the state estimate based on measurements and the system model.

2.3.2 Unscented Kalman filter algorithm

Just like the EKF, the UKF is an extension of the linear Kalman filter, designed to handle nonlinear systems and non Gaussian noise. Unlike the EKF, which linearizes the system dynamics using first order Taylor series expansion, the UKF approximates the probability distribution through a more sophisticated technique called the unscented transform. The unscented transform involves selecting a set of sigma points from the current state distribution, which is then propagated through the non-linear battery model to compute predicted mean and covariance estimates. These sigma points are carefully chosen to capture the true statistical moments of the state distribution, thereby mitigating the inaccuracies associated with linear approximation techniques used in the EKF. However, it's important to note that the increased accuracy of the UKF comes at the expense of higher complexity and computational cost. The UKF is defined as [12]

$$\mathcal{X}_{k|k-1} = \{\chi^i_{k|k-1}\}, \quad i = 0, 1, ..., 2n \tag{2.16}$$

where $\mathcal{X}_{k|k-1}$ are the sigma points at time k given measurements up to time $k-1$. The sigma points, together with the weighted mean and weighted covariance are calculated as

$$x_{(i)}(k \mid k-1) = \begin{cases} \hat{x}^i_{(k|k-1)} & \text{for } i = 1 \\ \hat{x}^i_{(k|k-1)} + \sqrt{(n+\lambda)P(k \mid k-1)} & \text{for } i = 2, \ldots, n+1 \\ \hat{x}^i_{(k|k-1)} - \sqrt{(n+\lambda)P(k \mid k-1)} & \text{for } i = n+2, \ldots, 2n+1 \end{cases} \tag{2.17}$$

$$W^m_{(i)} = \begin{cases} \frac{\lambda}{n+\lambda} & \text{for } i = 1 \\ \frac{1}{2(n+\lambda)} & \text{for } i \neq 1 \end{cases} \tag{2.18}$$

$$W^c_{(i)} = \begin{cases} \frac{\lambda}{n+\lambda} + \frac{1-\alpha^2+\beta}{2(n+\lambda)} & \text{for } i = 1 \\ \frac{1}{2(n+\lambda)} & \text{for } i \neq 1 \end{cases} \tag{2.19}$$

where n is the number of states, α, β and κ are tuning terms, λ is a term that describes the distance between the sigma point and the mean point, and is calculated as

$$\lambda = \alpha^2(n + \kappa) - n \tag{2.20}$$

In a normal distribution, α is equal to one, β is equal to two and κ equal to zero [34]. Each sigma point is then propagated through the state transition function to predict the potential states at the current time step

$$\chi^i_{k|k-1} = f(\chi^i_{k-1|k-1}, u_k), \quad i = 0, 1, ..., 2n \tag{2.21}$$

where $\chi^i_{k|k-1}$ are the sigma points propagated through the state transition function. These predicted states are used to compute the mean of the predicted states

$$\hat{x}_{k|k-1} = \sum_{i=0}^{2n} w_i^{(m)} \chi^i_{k|k-1} \tag{2.22}$$

where $\hat{x}_{k|k-1}$ is the predicted state estimate at time k given measurements up to time $k-1$ and $w_i^{(m)}$ are the weights for the mean. Next, the covariance matrix of the predicted states is computed

$$P_{k|k-1} = \sum_{i=0}^{2n} w_i^{(c)} (\chi^i_{k|k-1} - \hat{x}_{k|k-1})(\chi^i_{k|k-1} - \hat{x}_{k|k-1})^T + Q_k \tag{2.23}$$

where Q_k is the process noise covariance at time k, R_k is the measurement noise covariance at time k, $w_i^{(c)}$ are the weights for the covariance and $P_{k|k-1}$ is the predicted error covariance at time k. Then, the sigma points are transformed through the measurement function to predict the potential measurements at the current time step

$$\mathcal{Y}_{k|k-1} = \{\gamma^i_{k|k-1}\}, \quad i = 0, 1, ..., 2n \tag{2.24}$$

where $\mathcal{Y}_{k|k-1}$ are the transformed sigma points at time k given measurements up to time $k-1$, $\gamma^i_{k|k-1}$ are the transformed sigma points propagated through the measurement function. Using these transformed sigma points, the predicted measurement mean is calculated

$$\gamma^i_{k|k-1} = h(\chi^i_{k|k-1}), \quad i = 0, 1, ..., 2n \tag{2.25}$$

Now the predicted measurement mean can be calculated as

$$\hat{z}_k = \sum_{i=0}^{2n} w_i^{(m)} \gamma^i_{k|k-1} \tag{2.26}$$

where $\hat{z}_k$ is the predicted measurement at time k. With the predicted measurement determined the predicted measurement covariance can be determined

$$P_y = \sum_{i=0}^{2n} w_i^{(c)} (\gamma^i_{k|k-1} - \hat{z}_k)(\gamma^i_{k|k-1} - \hat{z}_k)^T + R_k \tag{2.27}$$

where P_y is the innovation covariance at time k. Next the cross covariance is calculated

$$P_{xy} = \sum_{i=0}^{2n} w_i^{(c)} (\chi^i_{k|k-1} - \hat{x}_{k|k-1})(\gamma^i_{k|k-1} - \hat{z}_k) \tag{2.28}$$

where P_{xy} is the cross covariance matrix. Using the cross covariance matrix and the innovation covariance, the Kalman gain is calculated

$$K_k = P_{xy} P_y^{-1} \tag{2.29}$$

where K_k is the Kalman gain at time k. With the Kalman gain, the state prediction is updated using the actual measurement at time k

$$\hat{x}_{k|k} = \hat{x}_{k|k-1} + K_k(z_k - \hat{z}_k) \tag{2.30}$$

where z_k is the actual measurement at time k. As a final step the error covariance is updated

$$P_{k|k} = P_{k|k-1} - K_k P_y K_k^T \tag{2.31}$$

where $P_{k|k}$ is the updated error covariance at time k. This iterative process provides an effective way to estimate states in nonlinear systems by efficiently propagating sigma points through the nonlinear functions while appropriately updating the mean and covariance estimates.

2.3.3 Observability on state space representation

The global observability criterion of the state space battery model used in Kalman filtering needs to be controlled by implementing the following formula

$$\mathcal{O} = \begin{bmatrix} C & CA & CA^2 & \cdots & CA^{n-1} \end{bmatrix}^T$$

to observe whether the system is controllable or not. If the observability matrix has fulfilled the rank condition then the system is globally observable from all modes. If the observability matrix does not fulfill the rank condition, then the system has

linear dependent rows resulting in a non observable system. If the system is non observable then the state space representation needs to be changed.

2.4 SOH estimation

While estimating the SOC of the battery is of utmost importance, estimation of the batteries health is also of interest [35]. As the battery is cycled up and down in SOC, it slowly degrades. This means that the battery will lose capacity over time, and this is important to estimate in order to improve the estimation of the SOC. The SOH provides valuable insights into a battery's long-term reliability and performance degradation. By continuously monitoring it, the gradual loss of capacity and power capability can be determined [9]. This degradation directly affects the accuracy and reliability of SOC estimation algorithms, as it supplies crucial information about the battery's present health status and remaining usable life.
There are various methods for estimating SOH for a battery, each with its own set of pros and cons. One commonly used approach is the internal resistance method, which relies on the principle that a battery's internal resistance changes over time as it undergoes cycles. By comparing the current resistance of a cycled battery to its rated or nominal resistance, typically obtained from datasheets or initial measurements when the battery was new, an estimation of SOH can be made. This method is advantageous for its simplicity and relatively good accuracy. However, it lacks the ability to provide a detailed projection of how the battery's health evolves over time. Another method, known as the battery capacity measurement method, works on the same principle as the internal resistance method, but instead of using the measured resistance of the battery, the capacity of the battery is measured and used for SOH estimation [36].

The last method, known as the OCV measurement method, involves measuring the battery's capacity during cycling and using this data to perform linear regression based on the number of cycles. The advantage of this method is that it gives a good estimate of SOH as well as it gives a function to estimate the projection of the battery health over time. A disadvantage of all these methods is that it takes a lot of time to complete as the battery needs to be cycled in order to extract the data [37].

2.5 SOP estimation

Accurate estimation of SOC and SOH enables precise estimation of SOP. This is important because it gives crucial information for the BMS in order to prevent overloading, as well as optimize the performance of the vehicle. Just as there exist numerous ways to estimate SOC and SOH, there also exist different options when estimating SOP. The most basic approach to SOP estimation is to only consider that power is equal to the terminal voltage multiplied by the maximum allowed current. This method is very simple and gives a grasp understanding of available power. The problem with this approach is that the maximum allowed current is only valid for

specific intervals in the SOC range. A battery cannot output power at maximum current when the SOC is very low for instance. Therefore more sophisticated models exist that tries to estimate the present maximum current. This is applicable for both discharging and charging processes. Specifically, if the SOC is low, then the maximum allowable discharge current would be lower than the maximum allowable charge current [38]. The disadvantage of these methods is that the estimation of the maximum allowed current for a given moment depends on several different factors and can be hard to estimate.

2.6 Battery cell thermal management

During charge and discharge heat is generated within the battery cell. The heat is generated due to ohmic (Joule heat) and non-ohmic (electrochemical processes) mechanisms within the cell. The heat is then transferred from the core through the different material layers out to the surface [13]. Batteries have a predefined optimal temperature range for which the cells should be operated in. If the cells are operated outside of this condition, the cell chemistry will be damaged leading to cell degeneration and in worst cases also battery thermal runaway. Once the thermal runaway has begun within one cell, it can not be stopped by itself and can therefore easily spread to other cells leading to toxic chemical release and in extreme cases fire explosions [13]. This results in that battery cells and battery packs need to be cooled or warmed to stay within the temperature regions. It is crucial for a BMS system to be able to handle heat management during charge and discharge, which results in the thermal changes within a cell need to be modeled [13].

3
Methods

3.1 Battery model

The three different battery modeling techniques compared in Table 3.1 have different characteristics and properties. The ECM method consists of a few electrical components, making it easy and clear to understand, compared to the electrochemical and black box methods. The ECM method is not as computationally heavy compared to the others and therefore is sufficient for automotive applications and Electronic Control Units (ECUs). The loss in accuracy of the ECM model compared to the other two methods can be slightly compensated by increasing the number of parallel links. Therefore, the ECM modeling approach was chosen for this thesis.

Table 3.1: Comparison of Battery Models [23].

Model name	Advantages	Disadvantages
ECM	Low computational cost and sufficient accuracy	Requires a large amount of measurement data
Black box	High accuracy	High computational cost, can't control the "black box"
Electrochemical	Models the real processes within the battery, high accuracy	High computational cost and complex

3.1.1 Equivalent circuit model

For the ECM, the number of RC links has to be determined. In [20], different numbers of RC links were tested against each other. The result was that two RC links were a sufficient choice for good accuracy and low complexity. Therefore, an ECM with two RC links was chosen for this project. The final electrical circuit can be seen in Figure 3.1.

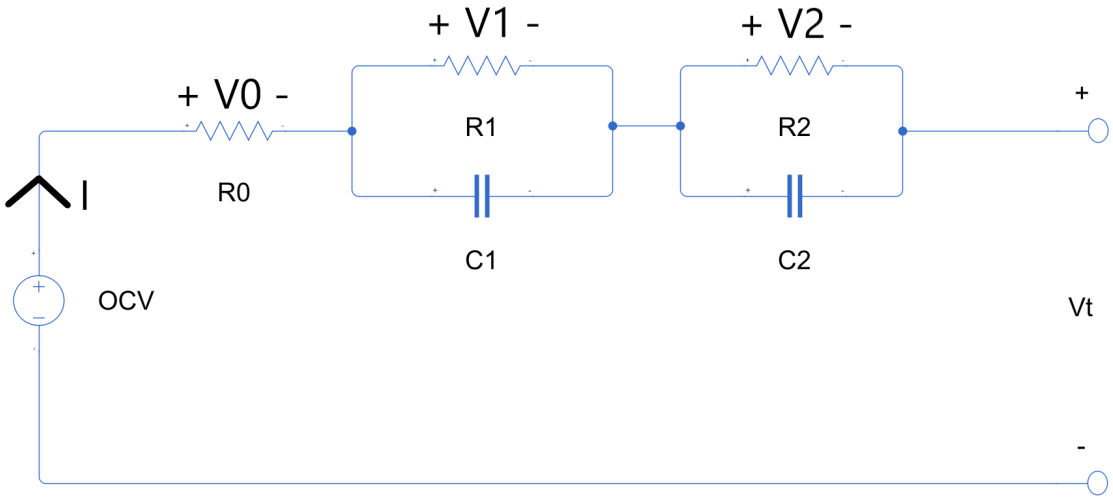

Figure 3.1: The chosen ECM.

By applying Kirchhoff's voltage law the terminal voltage $V_t(t)$ can be calculated as

$$V_t(t) = OCV(SOC((t)) - V_1(t) - V_2(t) - V_0(t) \tag{3.1}$$

Where $OCV(SOC(t))$ [V] is the voltage source, $V_1(t)$ [V] is the voltage drop over the first RC link, $V_2(t)$ [V] is the voltage drop over the second RC link, and $V_0(t)$ [V] is the voltage drop over the R_0 resistance. To calculate the dynamics of $V_0(t)$, $V_1(t)$ and $V_2(t)$ Kirchhoff's current law can be applied as

$$V_0(t) = R_0(t)I(t) \tag{3.2}$$

$$\dot{V}_1(t) = -V_1(t)\left(\frac{1}{R_1(t)C_1(t)} + \frac{\dot{C}_1(t)}{C_1(t)}\right) + \frac{1}{C_1(t)}I(t) \tag{3.3}$$

$$\dot{V}_2(t) = -V_2(t)\left(\frac{1}{R_2(t)C_2(t)} + \frac{\dot{C}_2(t)}{C_2(t)}\right) + \frac{1}{C_2(t)}I(t) \tag{3.4}$$

The state of charge of the battery is modeled with (2.7) and in this thesis, the Coulombic efficiency η is assumed to be 100%. With these equations the system can be modeled accurately while still maintaining low complexity.

3.1.2 State space representation

The derived equations can be represented by a state space model to simplify the implementation in Simulink. The input was selected to be the current $I(t)$, and the

output was selected to be the terminal voltage $V_t(t)$. The state space model was described with two states $V_1(t)$ and $V_2(t)$. With this decided the following state space model can be structured

$$x(t) = \begin{bmatrix} V_1(t) \\ \\ V_2(t) \end{bmatrix} \tag{3.5}$$

$$u(t) = I(t) \tag{3.6}$$

$$\dot{x}(t) = Ax(t) + Bu(t) \tag{3.7}$$

$$y(t) = Cx(t) + Du(t) + OCV(SOC(t)) \tag{3.8}$$

where

$$A = \begin{bmatrix} -\left(\frac{1}{R_1(t)C_1(t)} + \frac{\dot{C}_1(t)}{C_1(t)}\right) & 0 \\ \\ 0 & -\left(\frac{1}{R_2(t)C_2(t)} + \frac{\dot{C}_2(t)}{C_2(t)}\right) \end{bmatrix} \tag{3.9}$$

$$B = \begin{bmatrix} \frac{1}{C_1(t)} \\ \\ \frac{1}{C_2(t)} \end{bmatrix} \tag{3.10}$$

$$C = \begin{bmatrix} -1 & -1 \end{bmatrix} \tag{3.11}$$

$$D = -R_0(t) \tag{3.12}$$

3.1.3 ECM observability

The observability analysis of the battery model in Section 3.1.2 became

$$\mathcal{O} = \begin{bmatrix} C \\ \\ CA \end{bmatrix} = \begin{bmatrix} -1 & -1 \\ \\ \frac{1}{R_1(t)C_1(t)} + \frac{\dot{C}_1(t)}{C_1(t)} & \frac{1}{R_2(t)C_2(t)} + \frac{\dot{C}_2(t)}{C_2(t)} \end{bmatrix} \tag{3.13}$$

This matrix has full rank if the conditions $\frac{1}{R_1(t)C_1(t)} + \frac{\dot{C}_1(t)}{C_1(t)} \neq -1$ and $\frac{1}{R_2(t)C_2(t)} + \frac{\dot{C}_2(t)}{C_2(t)} \neq -1$ is not satisfied. The capacitive derivative fractions $\frac{\dot{C}_1(t)}{C_1(t)}$ and $\frac{\dot{C}_2(t)}{C_2(t)}$ were small and can be treated as zero, resulting in the matrix only losing full rank if $R_1(t)C_1(t) = R_2(t)C_2(t)$. This condition can not be fulfilled since $R_1(t)C_1(t)$ and $R_2(t)C_2(t)$ represent two different time constants and chemical phenomena within

the cell. The battery state-space representation was therefore observable and the available output measurement contains enough information to determine the internal voltage states of the system at any given time.

3.1.4 Implemented ECM

The battery model was based on (3.9), (3.10), (3.11), and (3.12) which was implemented in Simulink. The implementation can be seen in Figure 3.2.

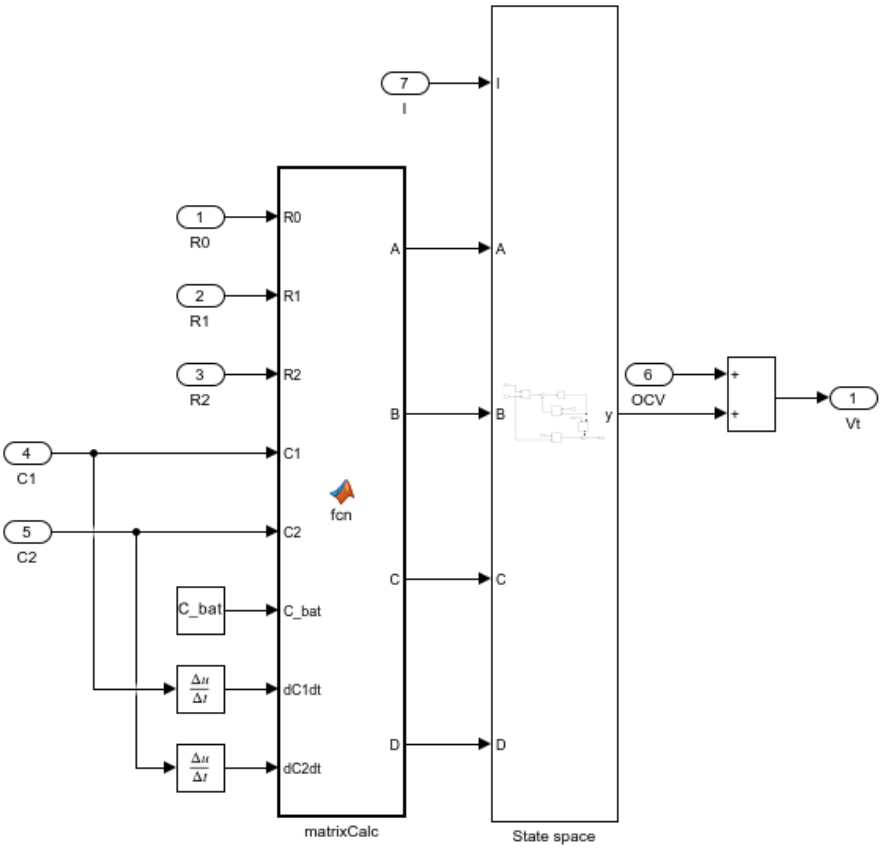

Figure 3.2: The implemented battery model with capacitance derivative in Simulink.

In the *matrixCalc* block, the state space matrices were formed using the specified inputs. In the *Statespace* block, a state space calculation was implemented. The OCV signal was added to the output of the state space block, forming the terminal voltage. With this setup the matrices in the state space could be updated at every time step.

3.2 Measurement campaign

In Table 3.3 the advantages and disadvantages of the different battery measurements techniques are shown. Both measurement techniques align with the usage of an offline parameter identification method. The time period of the thesis limits the number of measurements that can be done. Therefore, a measurement technique that was time effective and that had low complexity had to be used in order to have enough time to do all measurements and analyze the data. Therefore the DC pulse technique and SOC-OCV profiling methods were used The DC pulse technique was also selected doe to its high accuracy. The measurement and test equipment used can be seen in Table 3.2.

Table 3.2: Measurement Equipment.

Equipment type	**Equipment name**
Battery analyzer	Keysight E36731A
Battery charger	SKYRC MC3000
Voltage source	OJE PS3005
Multimeter	FLUKE 8846A
Temperature meter	ETAS ES650.1
Digital converter	ETAS ES600.1
Thermal chamber	Heraeus VOTSCH
Battery safety box	BATSAFE medium
4 wire measurement holder	ZKE battery holder

Table 3.3: Comparison of Battery Measurement Techniques.

Technique	Advantages	Disadvantages
EIS (Electrochemical Impedance Spectroscopy) [24]	High accuracy, don't affect the integrity of the battery	Battery model is usually determined by the measurement, high complexity, time-consuming, limited frequency range
DC pulses [27]	Battery models can be determined before measurements, high accuracy	Require large amount of measurement data, measurements are time-consuming, and affects the integrity of the battery

In order to form a model with high accuracy multiple temperature measurements were made. The temperatures chosen to test are -5 °C, 0 °C, 5 °C, 10 °C, 15 °C, 20 °C, 25 °C and 35 °C which all are within the design operating temperature conditions for both cell types. Since eight different temperatures were going to be investigated the measurement campaign took approximately 960 hours or 40 days. The battery charger cycled the cells as extensively as possible, ensuring continuous generation of data for SOH. The project utilized two types of batteries, the Molicel INR 21700 P42A (referred to as the 'grey cell' or 'grey') and the Lishen LR2170SA (referred to as the 'blue cell' or 'blue'), see Figure 3.4 and 3.3.

Figure 3.3: Lishen LR2170SA.

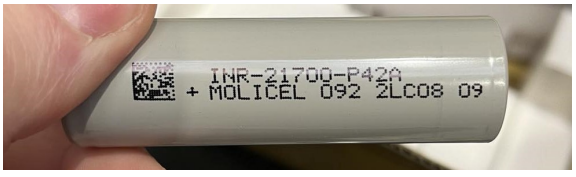

Figure 3.4: Molicel INR 21700 P42A.

Both of these batteries has a capacity of 4Ah which was beneficial as the tests will take the same duration of time, enabling a synchronized testing scheme. The Molicel cell has a maximum voltage of 4.2V and minimum voltage of 2.5V, while the Lishen cell has the same maximum voltage but a minimum voltage of 2.75V. To

obtain an accurate and reliable measurement of the battery cells, a ZKE four-wire measurement battery holder was used for current and voltage measurement. The holder can be seen in Figure 3.5.

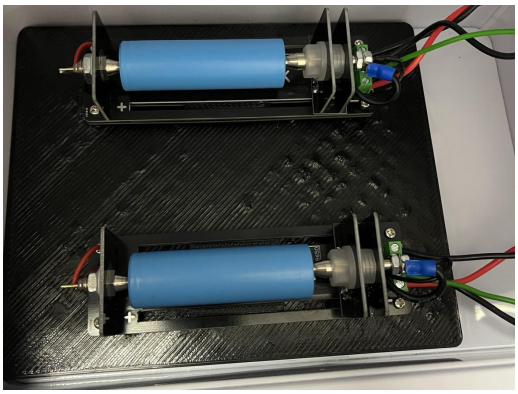

Figure 3.5: Two ZKE battery holders for the battery cells..

3.2.1 OCV-SOC profiling

The first measurement campaign consisted of a discharge and charge cycle, where the cell was drained from 100% SOC to 0%, and then 0% to 100% SOC to capture the OCV and SOC relation. This measurement was done with a constant discharge and charge current of C/20 where C is the C-rate current related to the battery capacity. The capacity of the two cells was $4Ah$ resulting in a C/20 current of $4/20 = 200mA$. The measurement was performed using the Keysight E36731A battery analyzer in Figure 3.8 together with the Keysight BenchVue Advanced Battery Test and Emulation software.

To ensure that the SOC was maintained at 100%, the cell was first charged to a maximum voltage of 4.2V with a constant current (CC) region. When the Keysight software detected that the battery had reached the maximum voltage, it switched to constant voltage (CV), where the current was ramped down until the minimum level was reached. However, the software does not provide the same functionality for maintaining 0% SOC value at a minimum voltage of 2.5V and 2.75V. To reduce the SOC to as close to 0% and the OCV to the rated minimum voltage, multiple discharge ramp down pulses with relaxation time were used. This measurement procedure was conducted for eight different ambient temperatures using the Heraeus Vötsch temperature chamber seen in Figure 3.6. To ensure that the battery cell had the same temperature as the temperature box, the battery cell was soaked inside the temperature chamber for at least two hours before any measurements started. To reduce the risk of hazardous gases and fire spread in case of a battery cell thermal runaway, the battery measurements were conducted inside of a battery safety box. The box used was the BAT-SAFE - Medium Lipo Charging Safe Box. The box has a filter that filters out the hazardous gas and particles and provides a closed environment so that the fire can't spread. The battery box used can be seen in Figure 3.7.

Figure 3.6: The temperature chamber used to capture the temperature dependency of the battery cells.

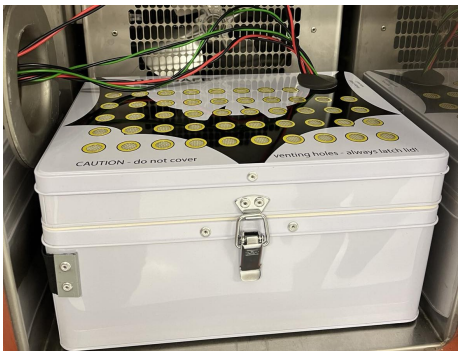

Figure 3.7: The battery box with the wiring harness going through the sealed hole.

3.2.2 DC pulses

The second campaign consisted of current pulses, where the cell was drained from 100% SOC to 10%, and then from 0% charged up to 90% SOC. The current pulses drains or charge the battery by 10% SOC, which is then followed by a relaxation time of one hour, where the cell slowly goes to its stable state, see Figure 2.5. In total nine discharge pulses and nine charge pulses were made. This was performed to capture the dynamics of the battery. Before any measurements, it was important to discharge the battery to as close as 0% SOC or charge it to as close to 100% as possible. To ensure this a CC-CV protocol was performed. The identical CC-CV method utilized for OCV-SOC profiling was also applied during this measurement. The Keysight instrument in Figure 3.8 was used for generating measurement data used for parameterization.

Figure 3.8: Two Keysight E36731A battery emulator and profiler.

3.2.3 Battery cycling

For the cycling of battery cells, the SkyRC MC3000 battery charger was used, which can be seen in Figure 3.9.

Figure 3.9: The SkyRC MC3000 used to cycle the battery cells.

As the Keysight instruments were conducting the OCV and pulse tests, the SkyRC MC3000 did the cycle tests in parallel, increasing the efficiency of the measurement campaign. The SkyRC MC3000 measured charge, terminal voltage, current and surface temperature during the cycling.

3.2.4 Thermal measurement

To verify cell surface temperature for the thermal model and temperature span for the ECM model, temperature measurements were added to the test rig, see Figure 3.10. The sensors were glued onto the battery surface, as shown in Figure 3.11, and positioned inside and outside the thermal chamber. The ETAS ES650.1 thermocouple with eight channels was coupled to four different sensors, and the voltage source OJE PS3005 powered the thermocouple and the analog-to-digital converter ETAS ES600.1. The temperature measurement ran in parallel with the DC pulse and OCV-SOC measurement to capture temperature differences on the battery cell surface and within the thermal chamber during the campaign. These measurements serve as benchmarks for the thermal model and validate temperatures for the eight different test conditions.

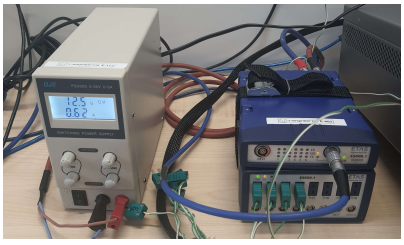

Figure 3.10: Temperature measurement equipment.

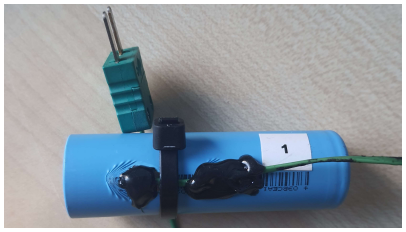

Figure 3.11: Cell with glued surface temperature sensor.

3.3 Parameter identification

The offline parameterization method was chosen for its alignment with data analysis and low computational cost, as shown in Table 3.4. The offline method has lower parameter accuracy and cannot capture time varying characteristics as effectively as the online method. Since the thesis was done concerning vehicle system design, the two battery models were designed with respect to the computational limits within a BMS ECU. This aspect makes the offline method using lookup tables for the parameters better suited.

Table 3.4: Comparison of Parameter Identification Methods [29].

Estimation technique	Advantages	Disadvantages
Online	Can handle time varying parameters to a large extent, Doesn't require lots of battery measurement	Computationally demanding, easily affected by initial parameters
Offline	Obtained from measurements, does not rely on real-time measurements, low computational cost	Parameter accuracy lacking, does not capture time-varying characteristics

The ECM described in Section 3.1.1 and shown in Figure 3.1 were implemented into the battery cell model, EKF and UKF to simulate the battery cell terminal voltage. These models use parameters based on the measurement data.

3.3.1 Voltage source parameterization

The OCV voltage source is a nonlinear function of SOC and is obtained by applying curve-fitting to the OCV-SOC measurement described in Section 3.2.1. The Matlab curve-fitting toolbox was used to obtain the ninth order polynomial OCV function. The SOC span was then divided into 100001 points and processed through the polynomial function to obtain corresponding OCV values which were subsequently

converted into a lookup table. Since the OCV function is temperature dependent, this procedure was repeated for all temperatures.

3.3.2 Series resistance parameterization

The series resistance R_0 parameterization was obtained from the DC-pulse measurement. The pulse train was divided up into nine SOC sections as depicted in Figure 2.5. The series resistance parameterization was then obtained by averaging the two resistive drop sections $U1$ - $U2$ and $U4$ - $U5$ using Ohm's law

$$\mathrm{R0} = \frac{\left(\frac{U1-U2}{I} + \frac{U3-U4}{I}\right)}{2} \tag{3.14}$$

where $U1$ corresponds to the point where the current pulses starts, and $U4$ corresponds to the point where it ends. $U2$ and $U3$ are design parameters chosen to represent the point where the series resistance drop ends and transitions into the time constant and RC link behavior. I corresponds to the magnitude of the current during the pulse. The R_0 values are then placed into a lookup table.

3.3.3 RC link parameterization

The two RC links in the ECM are parameterized by the voltage relaxation between point $U4$ and $U5$ by dividing the DC pulse measurement into nine parts as shown in Figure 2.5. The first RC link captures the fast response in the range of one to ten seconds, while the second RC link captures the more slow dynamics with a response of up to over 100 seconds. To capture the values for R_1, R_2, C_1 and C_2, a fitting function was used. This function was fitted against the measurement data using nonlinear least squares method *lsqcurvefit* in Matlab. The used fitting function was [14]

$$V_{relax}(t_r) = IR_1(1 - e^{-\frac{t_{\mathrm{pulse}}}{R_1C_1}})(1 - e^{-\frac{t_{\mathrm{r}}}{R_1C_1}}) + IR_2(1 - e^{-\frac{t_{\mathrm{pulse}}}{R_2C_2}})(1 - e^{-\frac{t_{\mathrm{r}}}{R_2C_2}}) \tag{3.15}$$

where t_{pulse} [s] is the duration of the current pulse, and t_r [s] is the relaxation time. The region between U_4 and U_5 was first normalized so that point U_4 starts at value zero. Then (3.15) was fitted against this curve, iterating the function with different values on R_1, R_2, C_1 and C_2, until the error between the measurement and the fitted curve was below a threshold value. Equation (3.15) was also used for the parameterization of the charge pulses, but in this case the relaxation region was inverted to fit the function.

3.4 SOC estimation methods

As described in Section **??** SOC cannot be directly measured, therefore, SOC has to be estimated. In vehicle applications the SOC is estimated in real time. Due to the electrochemistry and material constants the SOC behaves differently in different cells [13]. Therefore, all three SOC estimation methods listed in Table 3.5 will be

implemented and compared against each other. In the table the general advantages and disadvantages of the three methods are shown.

Table 3.5: Comparison of SOC Estimation Methods [12].

Estimation method	Advantages	Disadvantages
CC	Low complexity and computationally efficient, perfect accuracy in theory	Doesn't work well in practice as the estimation tends to drift over time due to measurement error
EKF	Great estimation performance, slightly lower computational cost than UKF	High complexity, hard to tune, high computational cost
UKF	Great estimation performance, Has a slight advantage over EKF due to better estimation of highly nonlinear systems	High complexity, hard to tune, high computational cost

3.4.1 Coulomb counting

CC (2.7) is one method for measuring the SOC of the battery over time. It works by measuring the battery current and integrating it over time. This method is highly effective and precise if the measurement has no bias or noise. The method tends to drift in accuracy due to measurement noise from real application sensors in vehicles, leading to inaccurate estimations. Therefore this method has to be recalibrated on a regular basis, for example by resetting the SOC to 100% when the battery has been determined to be fully charged.

3.4.2 Extended Kalman filter

The EKF described in Section 2.3 was implemented in Simulink. In order to implement the battery model in the EKF, several procedures had to be made. These are explained in detail in this section.

3.4.2.1 EKF discretization and Jacobian linearization

As the EKF runs in discrete time, the state space model had to be discretized to be implemented into the algorithms. The matrices described in Section 3.1.2 work as a starting point. Since the EKF will estimate the SOC, this had to be added as a state. This increases the complexity of the state space from a two state system to a three state system. Since the capacitance derivative term in the A matrix was a tricky term to have in an EKF, and since the term was close to zero, the term was neglected as a simplification. The discretization of a continuous time state space model was made by

$$x[k+1] = e^{AT_s}x[k] + A^{-1}(e^{AT_s} - I)Bu[k] \tag{3.16}$$

where $x[k]$ represents the state of the system at time k, $u[k]$ is the input at time k, A and B are system matrices, and T_s is the sampling interval. The matrix exponential e^{AT_s} can be challenging to compute directly, therefore Euler approximation was used to simplify the expression:

$$e^{AT_s} \approx I + AT_s \tag{3.17}$$

This approximation holds when the sampling interval T_s is small. Substituting the Euler approximation (3.17) into the state equation (3.16):

$$x[k+1] \approx (I + AT_s)x[k] + T_sBu[k] \tag{3.18}$$

Using the simplified discretization method, the new discrete state space was

$$x(k) = \begin{bmatrix} V_1[k] \\ V_2[k] \\ SOC[k] \end{bmatrix} \tag{3.19}$$

$$A_k = \begin{bmatrix} 1 - \frac{Ts}{R_1[k]C_1[k]} & 0 & 0 \\ 0 & 1 - \frac{Ts}{R_2[k]C_2[k]} & 0 \\ 0 & 0 & 1 \end{bmatrix} \tag{3.20}$$

$$B_k = \begin{bmatrix} \frac{Ts}{C_1[k]} \\ \frac{Ts}{C_2[k]} \\ \frac{-\eta T_s}{3600Q} \end{bmatrix} \tag{3.21}$$

$$C_k = \begin{bmatrix} -1 & -1 & OCV(SOC[k]) \end{bmatrix} \tag{3.22}$$

$$D_k = -R_0[k] \tag{3.23}$$

Once the model was discretized it could be linearized to be implemented into the EKF. Utilizing first-order Taylor linearization, (3.20), (3.21), (3.22) and (3.23) was linearized to

$$F_k = \begin{bmatrix} 1 - \frac{Ts}{R_1[k]C_1[k]} & 0 & 0 \\ 0 & 1 - \frac{Ts}{R_2[k]C_2[k]} & 0 \\ 0 & 0 & 1 \end{bmatrix} \tag{3.24}$$

$$G_k = \begin{bmatrix} \frac{Ts}{C_1[k]} \\ \frac{Ts}{C_2[k]} \\ \frac{-\eta T_s}{3600Q} \end{bmatrix} \tag{3.25}$$

$$H_k = \begin{bmatrix} -1 & -1 & \frac{dOCV(SOC[k])}{dSOC[k]} \end{bmatrix} \tag{3.26}$$

$$D_k = -R_0[k] \tag{3.27}$$

which was implemented into the Jacobian block in the EKF.

3.4.2.2 EKF initial state estimation and error covariance

The initial state conditions for the EKF include values connected to a specific starting condition. The states of the filter monitor the initial SOC, and initial polarization voltages of $U_1(0)$, $U_2(0)$. In the experiments and during measurements the SOC was started from the fully discharged or fully charged state. The two RC links can be assumed open initially resulting in no current passing through. Therefore the state estimation can be set to $\hat{x}_0 = [0\ 0\ 1]^T$ when assuming fully charged and $\hat{x}_0 = [0\ 0\ 0]^T$ when assuming fully discharged. The SOC estimation value can also be set to a value between 0 and 1 if another state that was not fully charged or discharged was assumed.

The initial error covariance matrix $P(0) = [\epsilon\ \epsilon\ \epsilon]^T$ is an estimation of how certain the user is about its initial state estimation $\hat{x}_0$ were each ϵ value of the matrix corresponds to the accuracy of the specific state. Both initial state estimation and error covariance matrix are directly entered into the prediction step resulting in them being posteriors to the first step. This yields that these two parameters are directly coupled to the initial Kalman filter performance hence they have to be selected with care.

3.4.2.3 EKF measurement and process noise covariance matrices

The Kalman filter has to be tuned with measurement error covariance matrix R and process error covariance matrix Q which is used to tune the trade off between measurements and modeling. The error covariance matrix Q for the EKF above is a 3x3 matrix where the diagonal elements correspond to how much the different states should be trusted within the motion model. A higher Q value indicates a more reliable state estimation from the motion model while lower Q values indicate less confidence in the motion model for the prediction. Using the following formula

$$Q_i = (x_{\text{meas}_i} - x_{\text{state}_i})^2 \tag{3.28}$$

where x_{meas_i} is the i-th value of the measured state and x_{state_i} is i-th the value of the modeled state, can be used as a starting point to find the magnitude of the parameter before tuning. The measurement covariance matrix R is used to tune how much the filter should trust the measurements. This design parameter is directly dependent on how noisy the measurements are. The behavior of R is inverse compared to Q resulting in that a high R value corresponds to a less reliable sensor measurement while a low R value indicates a more reliable sensor measurement. The total number of sensors and outputs within the system corresponds to the sizing of R. For the EKF model above will R be 1x1 since only one measurement (terminal voltage) is used. The size of the measurement error from the sensor is often used as guidance for the initial magnitude of R before tuning.

3.4.2.4 Observability of EKF model

The observability criteria stated in Section 2.3.3 were applied to the first order Taylor series linearized EKF battery model in order to examine if the system was locally observable. Since the system originally was nonlinear the observability criterion can only be examined around the operating point. This resulted in the following observability matrix:

$$\mathcal{O} = \begin{bmatrix} C \\ CA \\ CA^2 \end{bmatrix} = \begin{bmatrix} -1 & -1 & \frac{dOCV(SOC_0)}{dSOC} \\ \frac{1}{R_1[t]C_1[t]} & \frac{1}{R_2[t]C_2[t]} & 0 \\ -\frac{1}{R_1[t]C_1[t]} & -\frac{1}{R_2[t]C_2[t]} & 0 \end{bmatrix} \tag{3.29}$$

which were obtained by using Matlab syms-toolbox. This observability matrix has full rank if $\frac{dOCV(SOC_0)}{dSOC} \neq 0$ and $R_1[t]C_1[t] \neq R_2[t]C_2[t]$ conditions were fulfilled. The second condition was fulfilled since $R_1[t]C_1[t]$ and $R_2[t]C_2[t]$ represent two different time constants and chemical processes within the battery cell. However the first condition $\frac{dOCV(SOC_0)}{dSOC} \neq 0$ needs further investigation due to the SOC-OCV curve being nonlinear. This investigation can be determined by a rank test that involves Lie derivatives. This method was investigated in [39] and it was found that the system was locally observable around an operating point SOC_0 if and only if there exists a $k \in \mathbb{Z}$ such that

$$\left(\frac{d^k OCV}{dSOC^k}\right)(x_0) \neq 0 \tag{3.30}$$

has full column rank. This implies that the model was observable around the operating point if all derivatives of OCV are not equal to zero. This can be used in order to determine whether the first order linearization of the system was enough to claim observability or if higher order linearization terms need to be considered.

By investigating $\frac{dOCV(SOC_0)}{dSOC}$ in Figure 3.12 it can be seen that the derivative never was equal to zero, resulting in the linearized system being locally observable around the operating point.

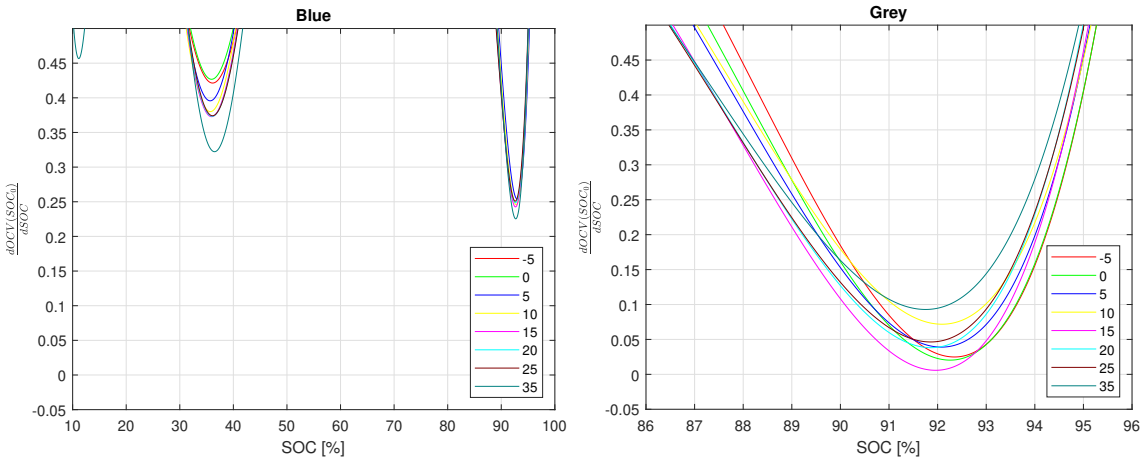

Figure 3.12: $\frac{dOCV(SOC_0)}{dSOC}$ for the blue and the grey cell.

3.4.2.5 EKF implementation in Simulink

The final system was implemented in Simulink and can be seen in Figure 3.13. In the Jacobian block (2.10) and (3.24) to (3.23) was implemented.

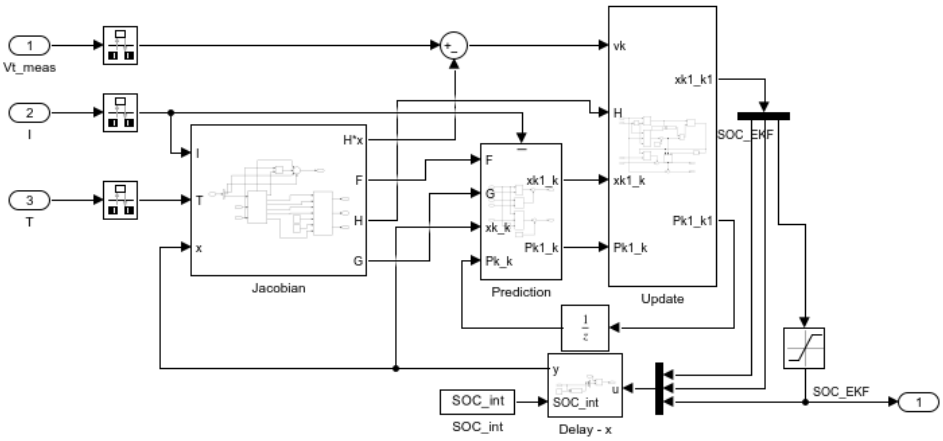

Figure 3.13: The implemented EKF in Simulink.

In the prediction block, (2.8) and (2.9) were implemented. (2.11) can be seen in the summation block that takes the $V_{t,meas}$ and $H * x$ signals. In the update block, (2.12) to (2.15) were implemented, completing all the governing equations for the EKF. To restrict the SOC estimate state (X_3), a saturation block was implemented, restricting the signal between zero and one.

3.4.3 Unscented Kalman filter

Another adaptation of the traditional Kalman filter is the UKF. This filter also handles nonlinearities just like the EKF but uses a different linearization method. While the EKF uses first order Taylor approximation, the UKF uses weighted sigma points to estimate the mean through the nonlinear model. This method better handles harder nonlinearities compared to EKF. It does not rely on a good linearization

estimate as the EKF does. In the algorithm, the sigma points are first predicted. These sigma points represent the potential states of the system at the current time step, given the measurements up to the previous time step.

The same initial state estimation and initial error covariance values were adapted for the UKF as for the EKF. The process and measurement noise initialization described in Section 3.4.2.3 were used. The tuning values of R and Q have a different impact on the UKF estimation compared to the EKF estimation, due to the different calculation methods within the filter algorithm for EKF and UKF. Therefore was the R and Q values changed and adopted for UKF performance.

3.4.3.1 UKF implementation in Simulink

The final system was implemented in Simulink and can be seen in Figure 3.14. In the sigma points block, (2.17), (2.18), (2.19) and (2.20) were implemented.

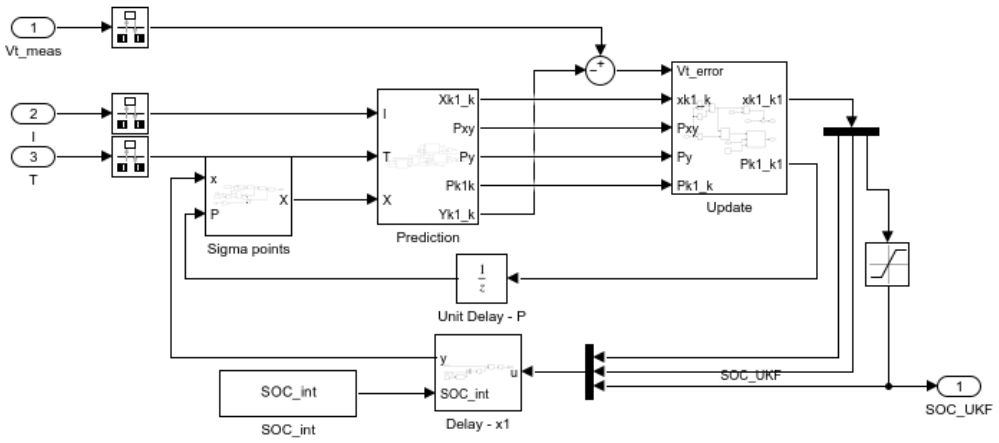

Figure 3.14: The implemented UKF in Simulink.

In the prediction block, (2.21) to (2.28) were implemented. In the update block, (2.23) and (2.29) to (2.31) were implemented. Just like with the EKF, the third state estimate was saturated between zero and one.

3.5 SOH estimation methods

There exist multiple methods for SOH estimation. Three common ways to estimate SOH can be found in Table 3.6, together with their advantages and disadvantages. The MC3000 used for SOH measurement could only measure changes in capacity and OCV with respect to a number of cycles. Therefore only OCV and capacity SOH estimation where methods examined in this project. Both methods were described in [37], and use linear regression to approximate the degradation.

Table 3.6: Comparison of SOH Estimation Methods [37].

Estimation method	Advantages	Disadvantages
Internal resistance measurement	Low complexity and computationally efficient	Takes a lot of time for measurements as the end-of-life resistance is needed
Battery capacity measurement	Low complexity and computationally efficient	Takes a lot of time for measurements as the end-of-life capacity is needed
OCV linear regression	Creates a function to estimate SOH depending on the number of cycles with the use of measured OCV	Higher complexity, Takes a lot of time for measurements

The first method uses the OCV after the cell has been fully charged and approximates the degradation based on how the OCV degrades. The other method uses the charged and discharged capacity to approximate the degradation. As the battery degrades, the OCV and capacity will decrease. The OCV and capacity value from the first cycle will represent 100% SOH. The current SOH value with respect to n numbers of cycles for OCV and capacity value will be calculated via (2.3) and (2.4). With the use of linear regression, the degradation can be estimated depending on how many cycles the battery has been run.

3.6 SOP estimation method

The SOP was obtained by implementing an analytic second-order SOP model based on a dual RC link model [40]. At each time step the maximum (I_{max}) and minimum (I_{min}) currents are calculated by utilizing maximum (V_{max}) and minimum (V_{min}) voltage values, which were battery parameters obtained from the data sheet. I_{max} and I_{min} was determined by modifying the current definition as stated in [40] Section 2.2, "Second-order SOP." This resulted in the following equations

$$I_{\max}(t) = \frac{(V_{\max} - V_t(t)) - R_0(t)I(t) - V_1(t)(1 - e^{-\frac{\Delta t}{R_1(t)C_1(t)}}) - V_2(t)(1 - e^{-\frac{\Delta t}{R_2(t)C_2(t)}})}{-(R_0(t) + R_1(t)(1 - e^{-\frac{\Delta t}{R_1(t)C_1(t)}}) - R_2(t)(1 - e^{-\frac{\Delta t}{R_2(t)C_2(t)}}))} \tag{3.31}$$

$$I_{\min}(t) = \frac{(V_{\min} - V_t(t)) - R_0(t)I(t) - V_1(t)(1 - e^{-\frac{\Delta t}{R_1(t)C_1(t)}}) - V_2(t)(1 - e^{-\frac{\Delta t}{R_2(t)C_2(t)}})}{-(R_0(t) + R_1(t)(1 - e^{-\frac{\Delta t}{R_1(t)C_1(t)}}) - R_2(t)(1 - e^{-\frac{\Delta t}{R_2(t)C_2(t)}}))} \tag{3.32}$$

where $V_1(t)$ and $V_2(t)$ were the estimated parallel voltages across the two RC links from the model, and $V_t(t)$ corresponds to the terminal voltage of the actual battery. Δt is a cautiousness parameter that tunes the maximum and minimum amplitude of $I_{max}(t)$ and $I_{min}(t)$ which affects how fast the system is allowed to reach the voltage levels. $P_{max}(t)$ $[W]$ and $P_{min}(t)$ $[W]$ are then calculated as

$$P_{\max}(t) = I_{\max}(t)\,(V_t(t) - R_0(t)(I_{\max}(t) - I(t))) \tag{3.33}$$

$$P_{\min}(t) = I_{\min}(t)\,(V_t(t) - R_0(t)(I_{\min}(t) - I(t))) \tag{3.34}$$

The SOP algorithm was implemented such that the algorithm limits and controls the current via

$$I(t) = \max(I_{\text{req}}(t), I_{\max}(t), I_{\text{lim,discharge}}) \tag{3.35}$$

for discharge and

$$I(t) = \min(I_{\text{req}}(t), I_{\min}(t), I_{\text{lim,charge}}) \tag{3.36}$$

for charge. $I_{req}(t)$ was the requested current, and $I_{lim,charge}$, $I_{lim,discharge}$ is the maximum charge and discharge current respectively, from the data sheet that must never be exceeded [40].

3.6.1 Predicted maximum power

A control system for an automotive application needs to know the future predicted maximum power in order to hold a power level for a given time horizon without lowering the power scope. This is useful for short term accelerations and overtakes. The concept of predictive maximum power for an RC link circuit model described in [40] was used and modified to fit for the model described in Section 3.1.1. Presuming that the controller mandates maximum discharge within a specified time horizon, the assumption $I(t) = I_{\max}(t)$ can be made. By applying that to (3.31), the following was obtained

$$I(t) = K((V_{\max} - V_t(t)) - \hat{V}_1(t)a(t) - \hat{V}_2(t)b(t)) \tag{3.37}$$

where,

$$a(t) = \left(1 - e^{-\frac{\Delta t}{R_1(t)C_1(t)}}\right) \tag{3.38}$$

$$b(t) = \left(1 - e^{-\frac{\Delta t}{R_2(t)C_2(t)}}\right) \tag{3.39}$$

and

$$K(t) = \frac{1}{-R_1(t)a(t) - R_2(t)b(t)} \tag{3.40}$$

$\hat{V}_1(t)$ and $\hat{V}_2(t)$ are defined as estimated voltage levels from the ECM model and were therefore not measurable. By expanding (3.37) with $V_t(t)$ it becomes

$$I(t) = K(t)(V_{\max} - OCV(t) - R_0(t)I(t) + V_1(t) + V_2(t) - \hat{V}_1(t)a(t) - \hat{V}_2(t)b(t)) \tag{3.41}$$

The following increments were introduced $\Delta I(t) = I(t) - I(t_0)$, $\Delta V_1(t) = V_1(t) - V_1(t_0)$, $\Delta \hat{V}_1(t) = \hat{V}_1(t) - \hat{V}_1(t_0)$, $\Delta V_2(t) = V_2(t) - V_2(t_0)$ and $\Delta \hat{V}_2(t) = \hat{V}_2(t) - \hat{V}_2(t_0)$. By assuming that the OCV remains unchanged and that the model accurately describes the voltage changes ($\Delta \hat{V}_1(t) \approx \Delta V_1(t)$) in (3.41) for initialization time t_0. t_0 can be subtracted from (3.41) resulting in

$$\Delta I(t) = I(t) - I(t_0) = K(t)R_0(t)\Delta I(t) + \Delta V_1(t)K(t)(1 - a(t)) + \Delta V_2(t)K(t)(1 - b(t)) \tag{3.42}$$

By putting it on the form

$$\Delta I(t) = -\tilde{K}_1(t)\Delta V_1(t) - \tilde{K}_2(t)\Delta V_2(t) \tag{3.43}$$

as suggested in [40] $\tilde{K}_1$ and $\tilde{K}_2(t)$ become:

$$\tilde{K}_1(t) = \frac{K(t)(a(t) - 1)}{1 - K(t)R_0(t)} \tag{3.44}$$

$$\tilde{K}_2(t) = \frac{K(t)(b(t) - 1)}{1 - K(t)R_0(t)} \tag{3.45}$$

By having the equations on the same standardized form as shown in [40] the following equations

$$\tilde{T}_1(t) = \frac{R_1(t)C_1(t)}{1 + R_1(t)\tilde{K}_1(t)} \tag{3.46}$$

$$\tilde{T}_2(t) = \frac{R_2(t)C_2(t)}{1 + R_2(t)\tilde{K}_2(t)} \tag{3.47}$$

and

$$v_1^*(t) = \frac{R_1(t)I(t) - \hat{V}_1(t)}{1 + R_1(t)\tilde{K}_1(t)} \tag{3.48}$$

$$v_2^*(t) = \frac{R_2(t)I(t) - \hat{V}_2(t)}{1 + R_2(t)\tilde{K}_2(t)} \tag{3.49}$$

from Section 2.3, "Predicted maximum power" can directly be used. The future maximum current and voltage are calculated as

$$I(t + \tau) = I_{\max}(t) - \tilde{K}_1(t)v_1(t)^*(1 - e^{-\frac{\tau}{\tilde{T}_1}(t)}) - \tilde{K}_2(t)v_2(t)^*(1 - e^{-\frac{\tau}{\tilde{T}_2(t)}}) \tag{3.50}$$

$$\begin{aligned} v(t + \tau) = {} & v(t) - R_0(t)\left(I_{\max}(t) - I(t)\right) \\ & + v_1(t)^{(1 - R_0(t)\tilde{K}_1(t))}\left(1 - e^{-\tau/\tilde{T}_1(t)}\right) + v_2(t)^{(1 - R_0(t)\tilde{K}_2(t))}\left(1 - e^{-\tau/\tilde{T}_2(t)}\right) \end{aligned} \tag{3.51}$$

The predicted maximum power for a given time horizon τ can be calculated by multiplying (3.50) with (3.51).

3.7 Thermal modeling

The thermal model utilized in this thesis will solely account for the voltage drop caused by the electrical components as a form of power loss, presuming that all energy is converted into heat. It will not consider any residual current flow released by the capacitors when the circuit is open. The power loss produced by the battery was calculated as

$$P_{loss}(t) = (OCV(SOC((t)) - V_t(t))I(t) \tag{3.52}$$

To obtain the heat generated, the power loss was integrated

$$Q_{hg}(t) = \int P_{loss}(t)dt \tag{3.53}$$

The heat dissipation was calculated using the surface area of the cell, and an assumption of the thermal conductivity of the battery cell

$$Q_{dis}(t) = \int ((T_{cell}(t) - T_{amb}(t))Ah)\, dt \tag{3.54}$$

where A is the surface area of the cell $[m^2]$, h is the heat transfer coefficient $[W/(m^2K)]$, T_{cell} is the cell temperature $[K]$ and T_{amb} is the ambient temperature $[K]$. The heat transfer coefficient has to be extracted by comparing simulated cell temperature and measured cell temperatures. The heat transfer coefficient is usually around 5-50 for lithium ion batteries [41]. The temperature change can be calculated using the mass of the battery cell and the specific heat capacity as

$$\Delta T(t) = \frac{Q_{hg}(t) - Q_{dis}(t)}{m_{cell}C_p} \tag{3.55}$$

where m_{cell} is the mass of the battery $[kg]$, and C_p is the specific heat capacity $[J/(KgK)]$. Just like the heat transfer coefficient, the specific heat capacity can be extracted by comparing simulated and measured cell temperature. The specific heat capacity for a lithium ion cell is around 800-1100 $J/(kgK)$ [42]. By adding the ambient temperature with (3.55), the temperature change of the battery cell was calculated as

$$T_{cell}(t) = T_{amb}(t) + \Delta T(t) \tag{3.56}$$

The calculated cell temperature was then looped back to (3.54) in order to update the temperature state of the system.

3.8 Validation

To test the models robustness and performance two different methods were used. To test the performance of the model compared to measurement data, the root mean

square error (RMSE) was used, described in Section 3.8.1. To test the robustness of the model a current cycle will be used. The cycle will stress test the model as the cycle contains nonlinear components which was more demanding to simulate. The current cycle used is described in Section 3.8.3.

3.8.1 Root mean square error

RMSE is a metric commonly used to evaluate the accuracy of a predictive model. It measures the average magnitude of the differences between simulated values and measured values. The RMSE was calculated using the following formula

$$\text{RMSE} = \sqrt{\frac{1}{n}\sum_{i=1}^{n}(y_i - \hat{y}_i)^2} \tag{3.57}$$

Where n is the number of data points, y_i is the measured value at index i, $\hat{y}_i$ is the simulated value at index i. The RMSE provides a single number to summarize the goodness of fit of a model. A lower RMSE indicates better agreement between simulated and measured values, while a higher RMSE suggests poorer performance.

3.8.2 Percentage error

As a complement to RMSE was also percentage error used. It measures the accuracy as the relative difference between the measured and prediction value [43]. The errors were calculated using

$$\text{Percentage Error}_i(\%) = \left|\frac{y_i - \hat{y}_i}{y_i}\right| \times 100\% \tag{3.58}$$

Where y_i is the measured value at index i, $\hat{y}_i$ is the simulated value at index i. A lower percentage value indicates a more accurate prediction [43].

3.8.3 Current cycle

In order to validate and test the models robustness a standardized driving cycle will be used. Specifically, the worldwide harmonized light duty vehicle test procedures (WLTP) will be used. WLTP is a standardized driving cycle used internationally in order to check the performance of vehicles, motors, and systems related to the vehicle. The standard WLTP cycle is 1750 seconds or 29 minutes and 10 seconds. The high dynamic components of the WLTP cycle made it an ideal choice for testing the robustness and performance of the battery model, along with evaluating the Kalman filters and the thermal model. The cycle will stress test the model to its limits. The WLTP cycle found in [44] was used and modified to test the cells. The unmodified WLTP cycle can be seen in Figure 3.15.

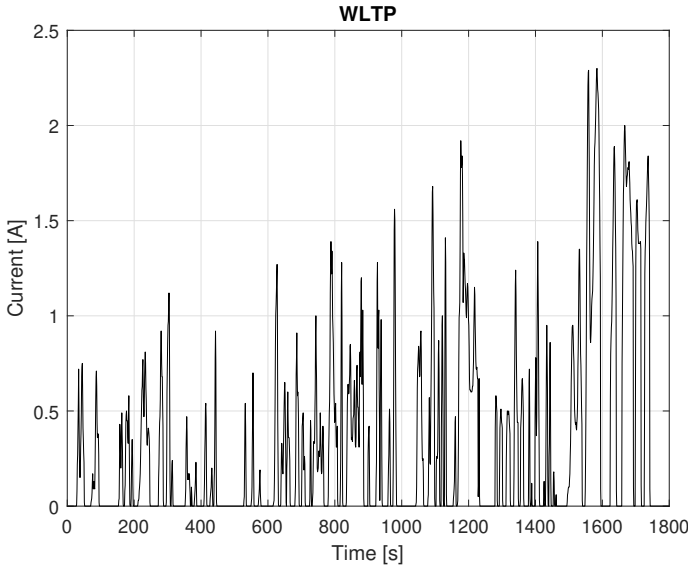

Figure 3.15: The unmodified WLTP cycle taken from [44].

Due to limitations both in the rated discharge current for the cells and also in the Keysight software, the WLTP current cycles were modified for the two cells. For the blue cell, the max discharge current was 12A. For the grey cell, the max discharge current is 45A. The WLTP cycle was modified so the max current of 45A is not vanish. Since the Keysight instrument was only able to draw 20A, all the peaks that exceeded this limit were cut to 20A. The resulting current cycle for both cells can be seen in Figure 3.16.

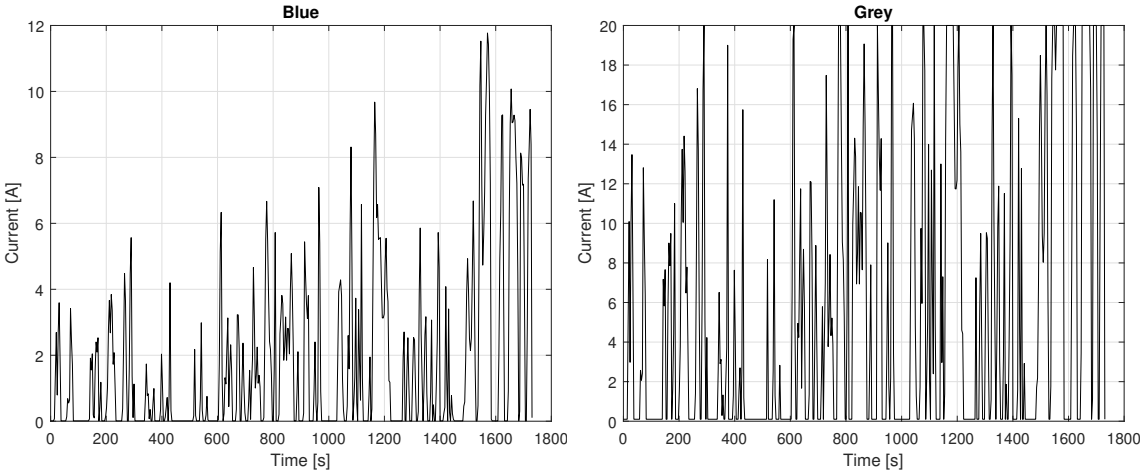

Figure 3.16: WLTP cycles used for the blue and the grey cell.

4
Results & Discussions

4.1 Battery measurement results

The OCV was measured and analyzed for two different cells at eight different temperatures. By observing Figure 4.1 it can be seen that the average OCV of charge and discharge OCV vary for the eight different temperatures, indicating a temperature dependency. However, there is a notable difference in OCV behavior between the blue and the grey cell. The grey cell consistently outputs the same curvature for all temperatures. The general trend is that OCV curvature at higher temperatures tends to result in a slightly lower voltage value, see Figure 4.2. There are some variations in measurements and these are most likely due to temperature deviations within the thermal chamber since its accuracy lies within ±1.5°C.

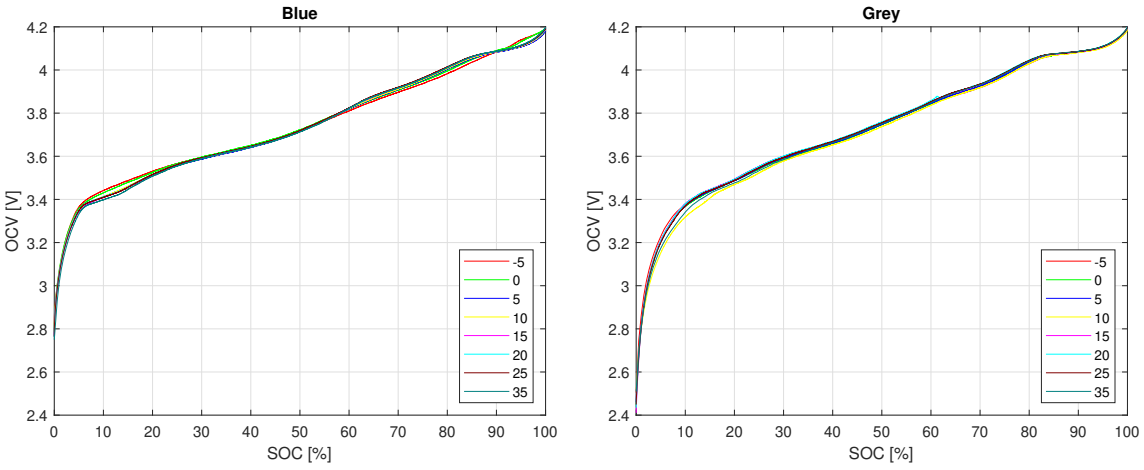

Figure 4.1: OCV averages for the blue and the grey cell at eight different temperatures [°C].

The blue cell has a different OCV behavior compared to the grey. There is a larger difference in OCV between the highest and lowest temp for blue compared to grey. The larger OCV difference between the temperatures will affect the modeling accuracy since the resolution for blue cell will be lower than for grey. The specific curvature of the OCV curve has to do with the manufacturing process and what type and amount of materials that have been used. This can clearly be seen since the blue and grey cell has two different voltage characteristics. In Figure 4.2, the voltage difference between charge and discharge for the highest and lowest temperature can be seen.

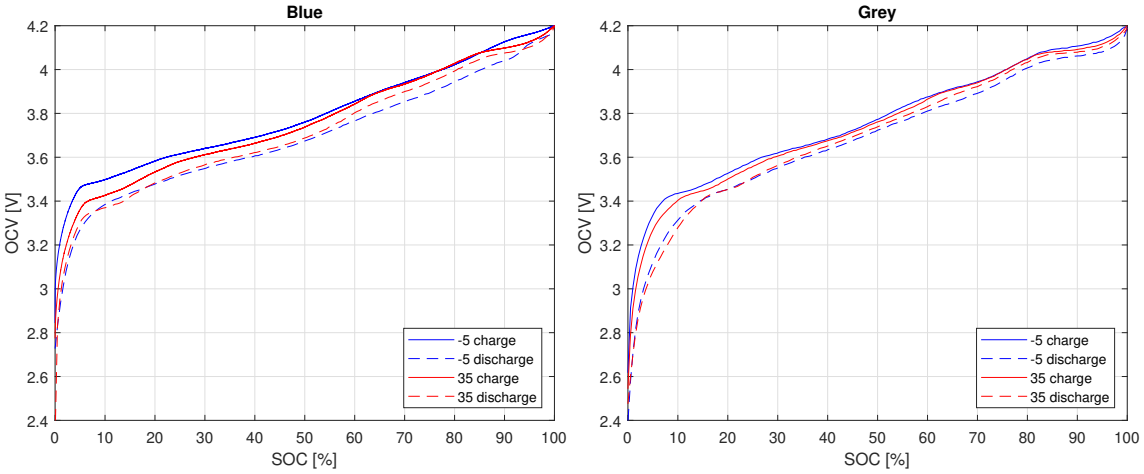

Figure 4.2: Discharge and charge OCV for blue and grey cells at highest and lowest measurement temperatures [°C].

The difference between charge and discharge for the temperatures of the grey cell is small. This small difference indicates that a higher temperature value within the test range could possibly be used without losing significant accuracy. On the other hand the blue cell provides measurements with larger differences. This indicates that it needs more temperature steps than the grey cell in order to provide good OCV resolution for the model. For both of the cells, it can be seen that the difference between charge and discharge is larger for -5°C compared to 35°C. This is due to that the internal resistance within the cell rises with colder temperatures, as it is harder for the ions to travel through the electrolyte.

4.2 Parameter identification

In Figure 4.3 OCV for 25°C charge, discharge and average are shown for both cells. The temperature of 25°C was selected to demonstrate the typical OCV characteristics of the blue and grey battery cells. The average OCV value for each temperature has been used for OCV parameterization to the battery model.

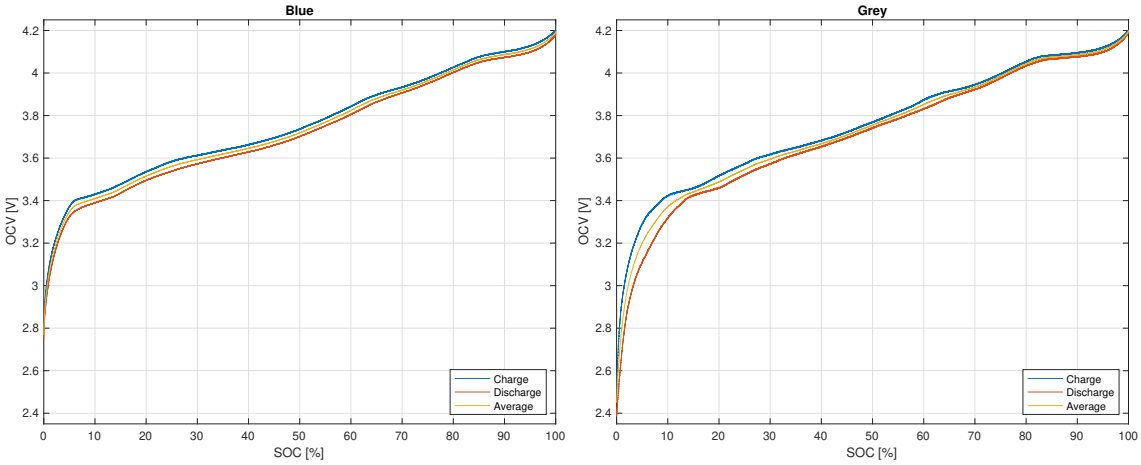

Figure 4.3: OCV average for the blue and the grey cell at 25°C.

The polynomial curve fitting of the grey cell OCV average is illustrated in Figure 4.4. The curve fit closely follows the OCV curvature, demonstrating that the selected method does not overestimate its values. This is evident since the OCV measurement includes sensor noise, yet the curve fit has not brought noise into its function.

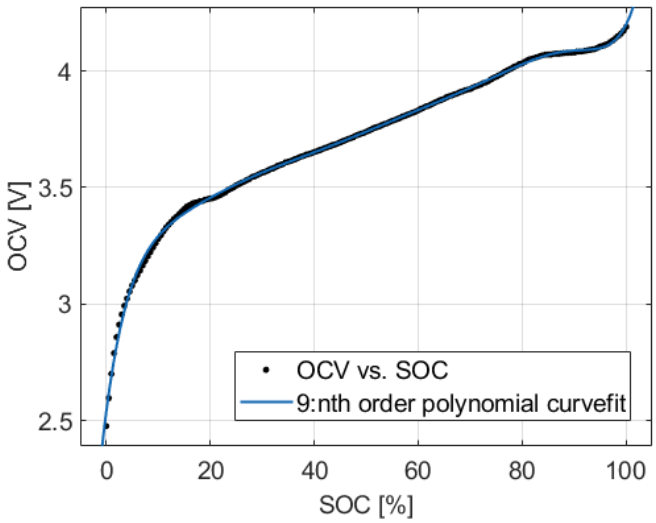

Figure 4.4: Matlab Curve Fitter toolbox to identify the fitted function.

By looking to the left at Figure 4.5 and 4.6 it is clearly seen that the curve fitting algorithm (3.15) accurately identifies U1, U2, U3 as well as the relaxation interval from U4 to U5. It can also be seen to the right that the algorithm correctly outputs

a curve fit in the U4 to U5 region for both charge and discharge. The fitting method does not overfit since the measurement noise is not present in the curve fit. This fitting procedure has been done for all eight temperatures both charge and discharge and the corresponding values for $C1$, $C2$, $R1$, and $R2$ have been saved into look up tables with respect to temperature and SOC level. The charge pulses utilizes the same fitting function as the discharge but the values in segment U4 to U5 are inverted.

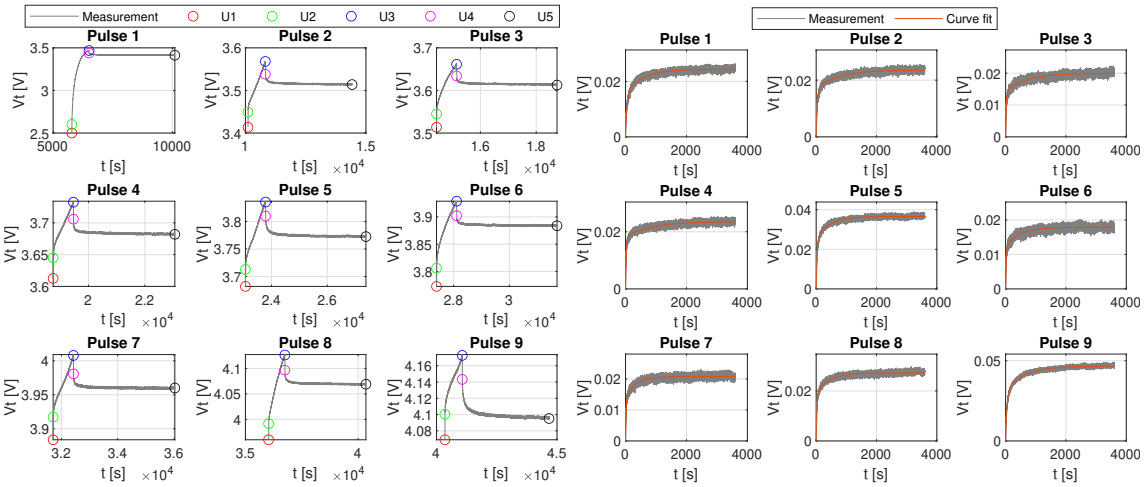

Figure 4.5: Charge parameter identification and curve fit for the grey cell at 25°C.

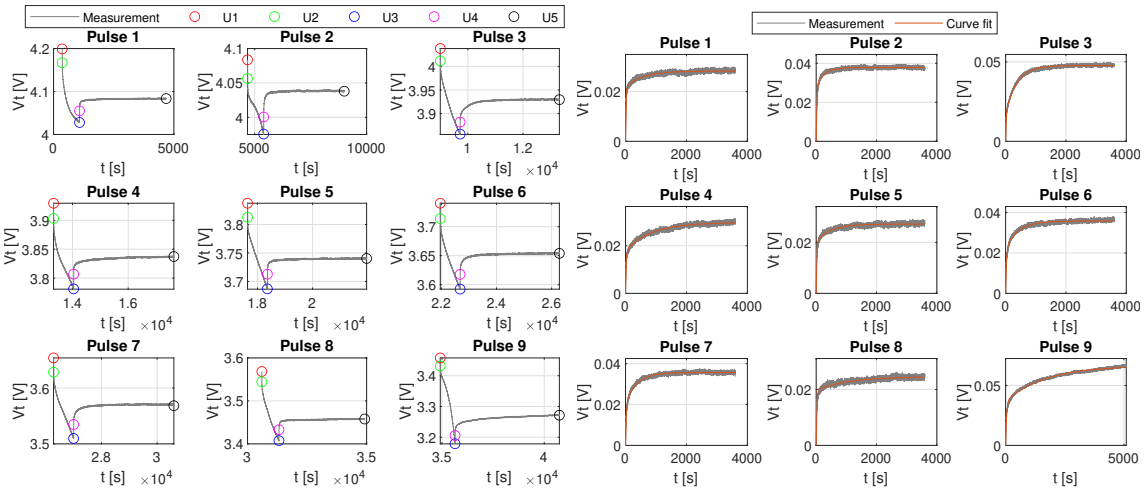

Figure 4.6: Discharge parameter identification and curve fit for the grey cell at 25°C.

From the parameter identification the parameters extracted for the blue cell can be seen in Figure 4.7 and Figure 4.8.

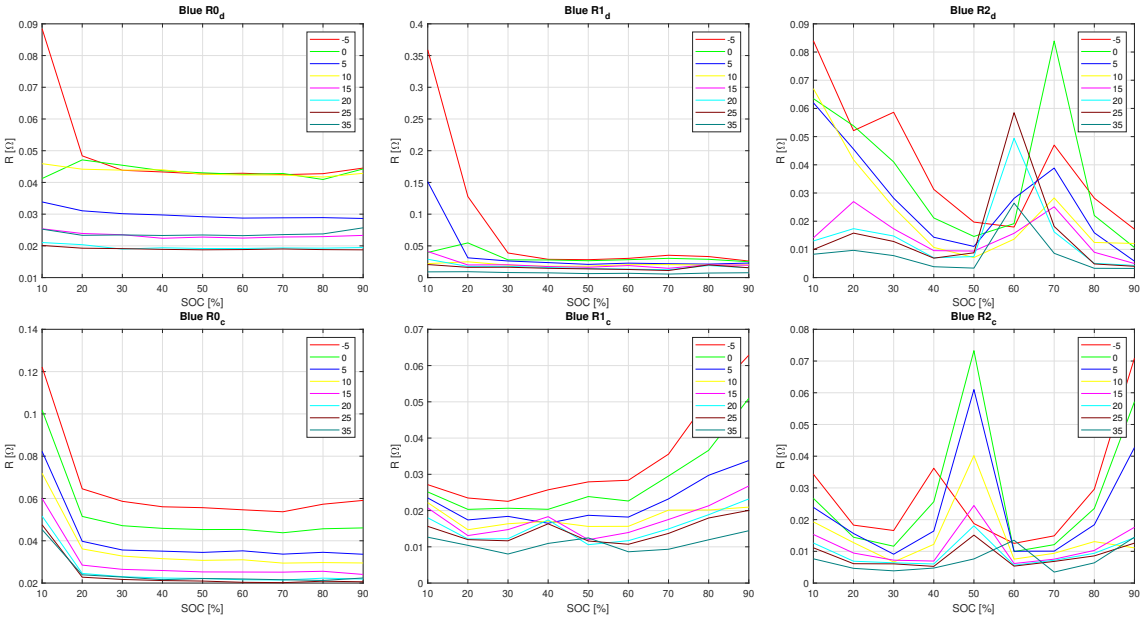

Figure 4.7: The resistance parameters for the blue cell.

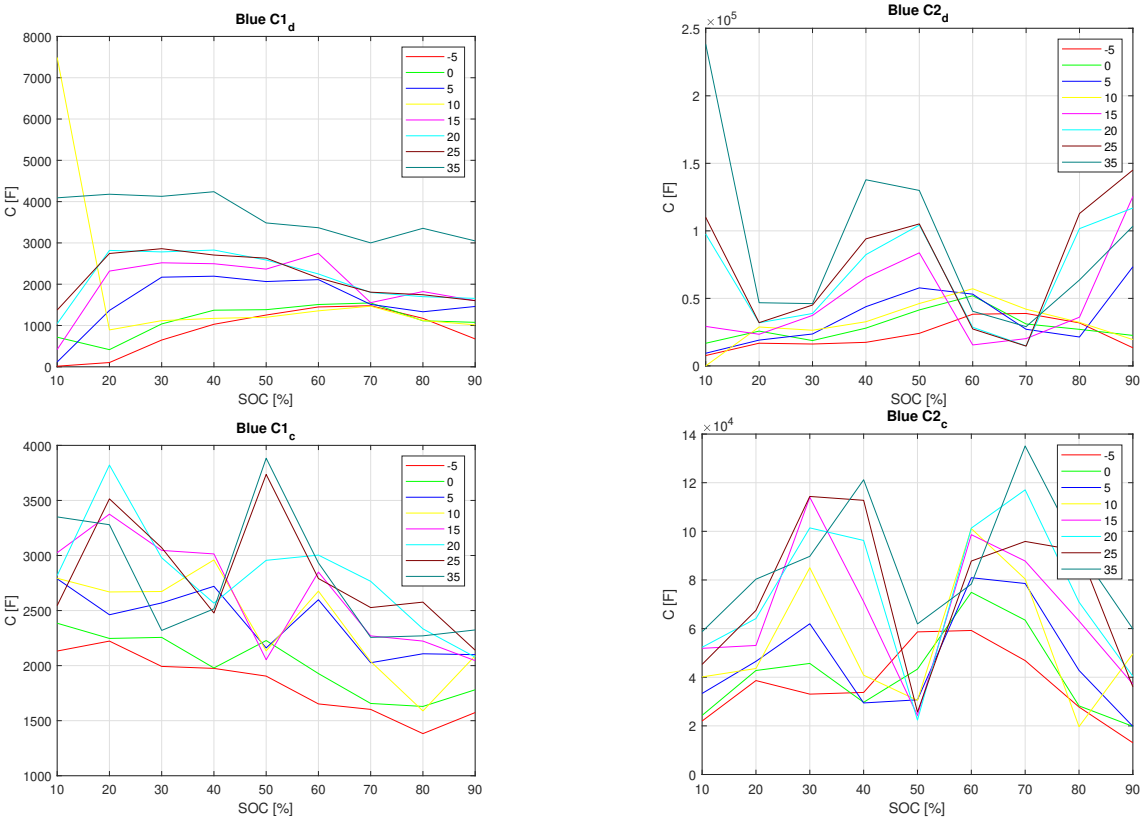

Figure 4.8: The capacitance parameters for the blue cell.

Some expected trends is that the resistance in the cell increases with decreasing temperature. It can also be seen that the resistance usually has its peaks at the ends of the SOC range. This is due to multiple factors related to the internal processes

inside the battery. When discharging it could for instance be due to decreased ion mobility, and when charging a potential explanation could be saturation of the active material. The parameters for the grey cell can be seen in Figure 4.9 and in Figure 4.10.

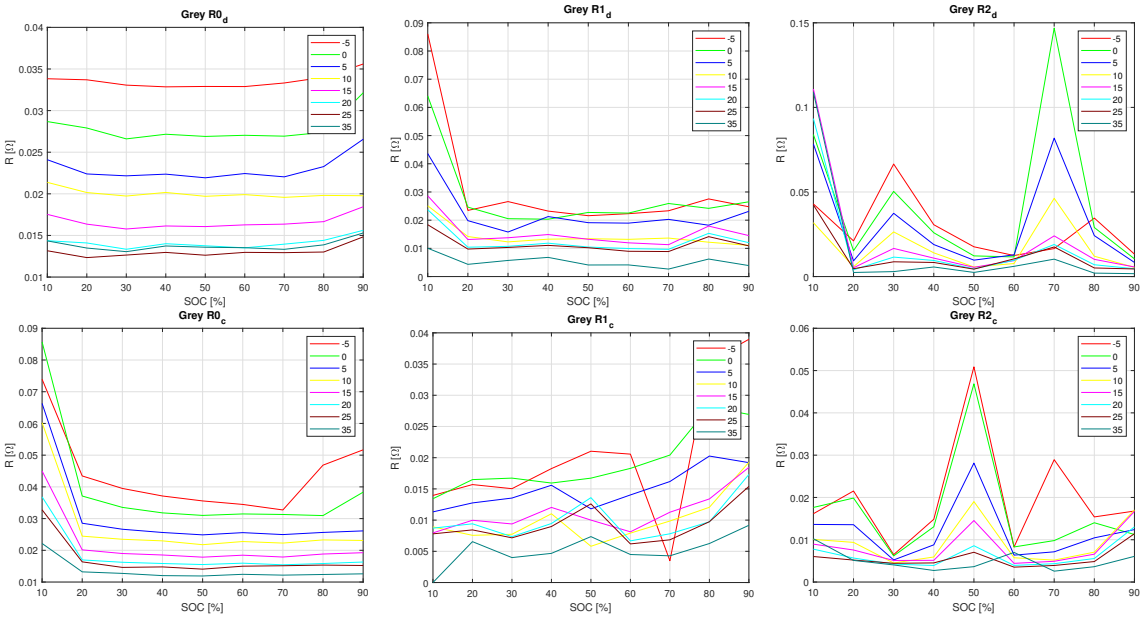

Figure 4.9: The resistance parameters for the grey cell.

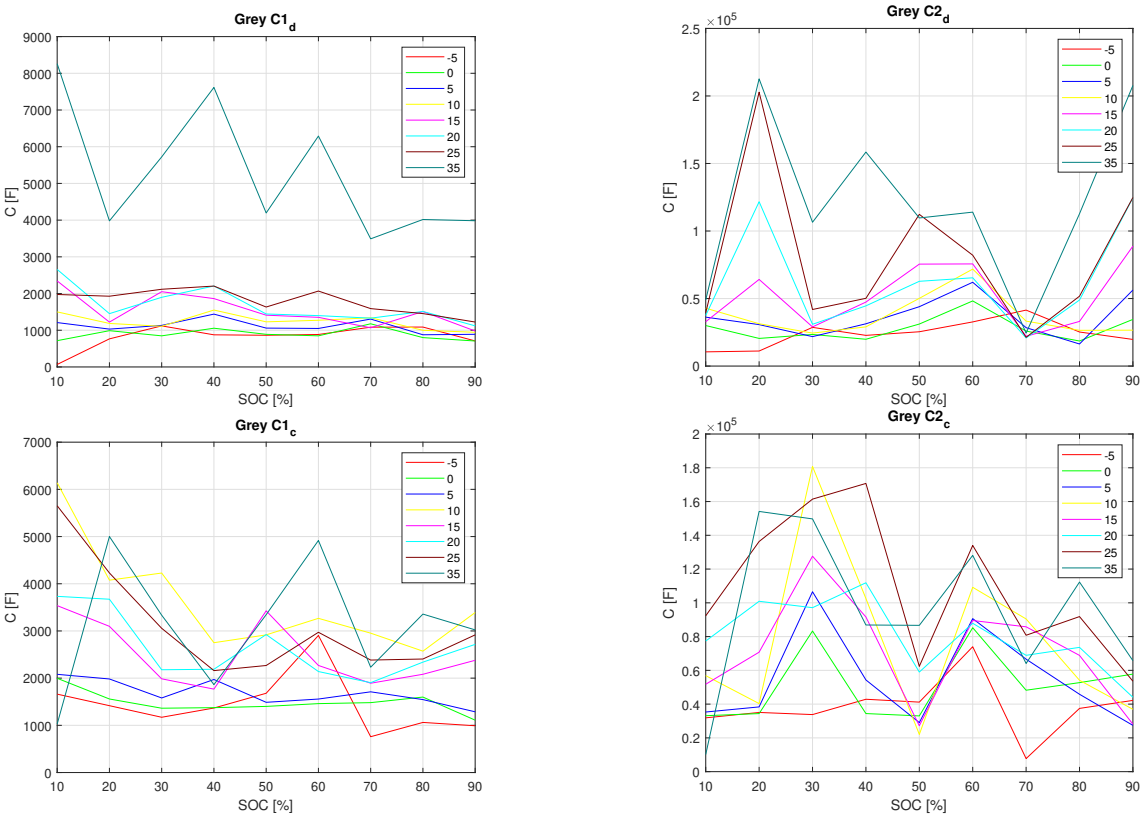

Figure 4.10: The capacitance parameters for the grey cell.

The same phenomenon is observed for the grey cell, wherein the resistance values peak at the lowest temperature. An outlier is noticeable for the $C1_d$ value at 35°C. This could be due to inaccurate curve fitting. However, upon simulating this temperature, the model behaves as expected, which would suggest that the parameter values are correct. It can also be seen that the parameters for the grey results in a lower impedance which is reasonable since the grey cell is rated for a higher C-current.

4.3 Battery ECM

The dual RC ECM described in Section 3.1 was run with the measured current profile used for charge and discharge measurements in order to simulate and compare the terminal voltage V_t from the model with the measured battery voltage. These types of simulations and measurement comparisons were conducted for all eight temperatures. The temperature of 25°C was selected to demonstrate the typical charge and discharge characteristics of the blue and grey battery cells. The comparison between the measurement and simulation of the two cells can be seen in Figure 4.11 and 4.12.

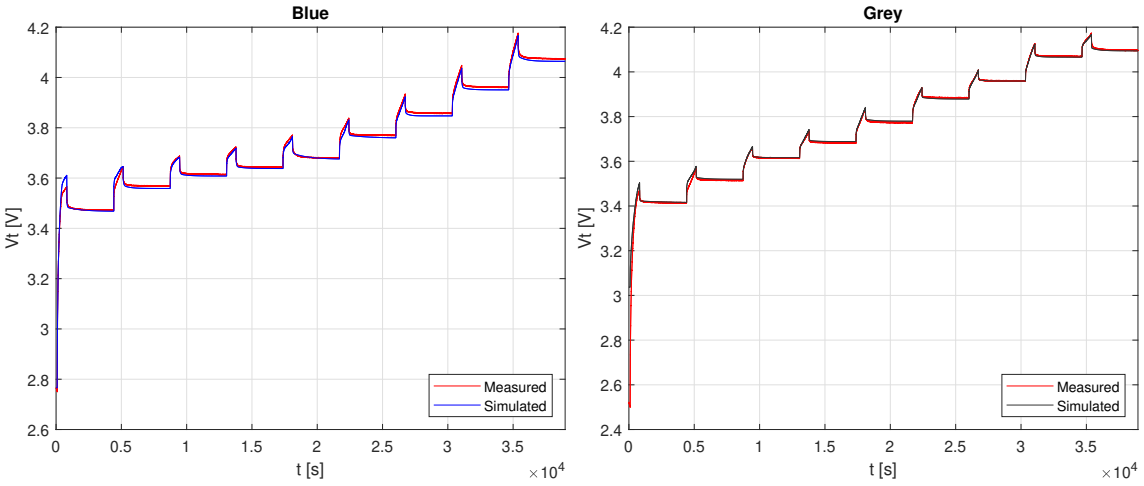

Figure 4.11: Comparison of measured and estimated charge terminal voltage for blue and grey cell at 25°C.

By looking at Figure 4.11, it can be seen that the simulated terminal voltage V_t aligns well with the measured output during charging for both cell chemistries. The model finds the right OCV value at every relaxation part which indicates that the OCV measurement has been done with a C-rate that has kept the internal chemistry close to the actual OCV. There are minor deviations in the relaxation parts. These deviations are most likely affected by the choice of ECM with only two RC links and the parameterization limitations within the chosen method.

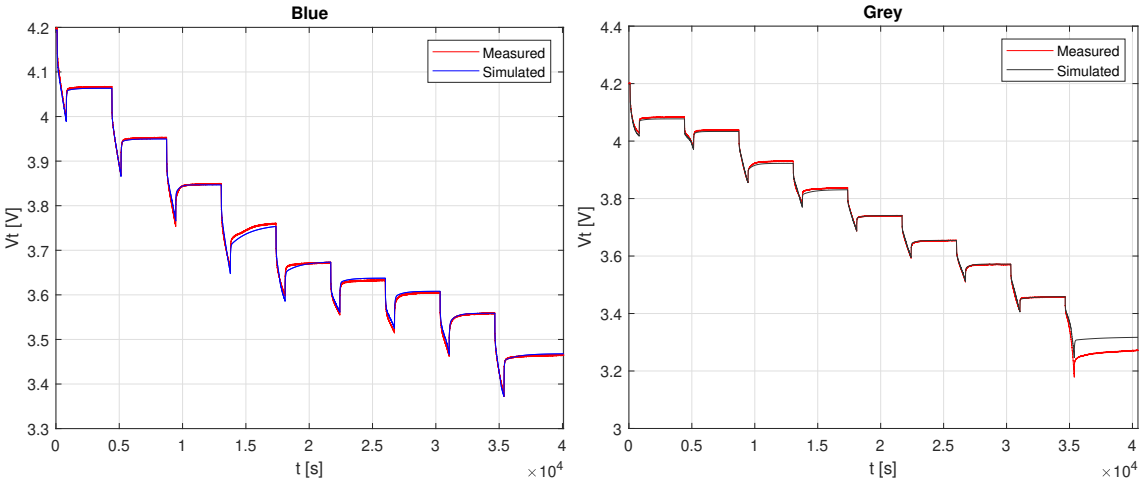

Figure 4.12: Comparison of measured and estimated discharge terminal voltage for blue and grey cell at 25°C.

However, in Figure 4.12, there is a deviation in finding the correct OCV value for the grey ninth pulse during discharge relaxation. By investigating the measurement from this region, it can be observed that the voltage has a trend of continuing to rise during relaxation. This indicates that the relaxation time of the grey cell for the ninth pulse needs a longer relaxation time in order for the chemistry to stabilize and reach the correct OCV value. Thereby there is a measurement error that affects the model via the parameterization. However, the blue cell has no modeling error within that region. This indicates that the relaxation time used for the blue cell was long enough for the chemistry to stabilize, and confirms that the model is functioning correctly as it provides the correct terminal voltage.

4.3.1 ECM with and without capacitance derivative

Two different ECM state space representations were evaluated, where the difference lies in the inclusion or exclusion of a capacitance derivative term when simulating the voltages V_1 and V_2 across the two parallels, see Figure 3.1. When solving the equations for the voltages in the ECM circuit, two capacitance derivatives of C_1 and C_2 were added due to the chain rule, see (3.3) and (3.4). To reduce the complexity of the model, it was investigated whether the derivatives can be excluded without significantly affecting the modeling performance. By comparison it can be seen in Figure 4.13 that both models perform well. There are some regions where both methods under and overestimates the different time constants for both cells.

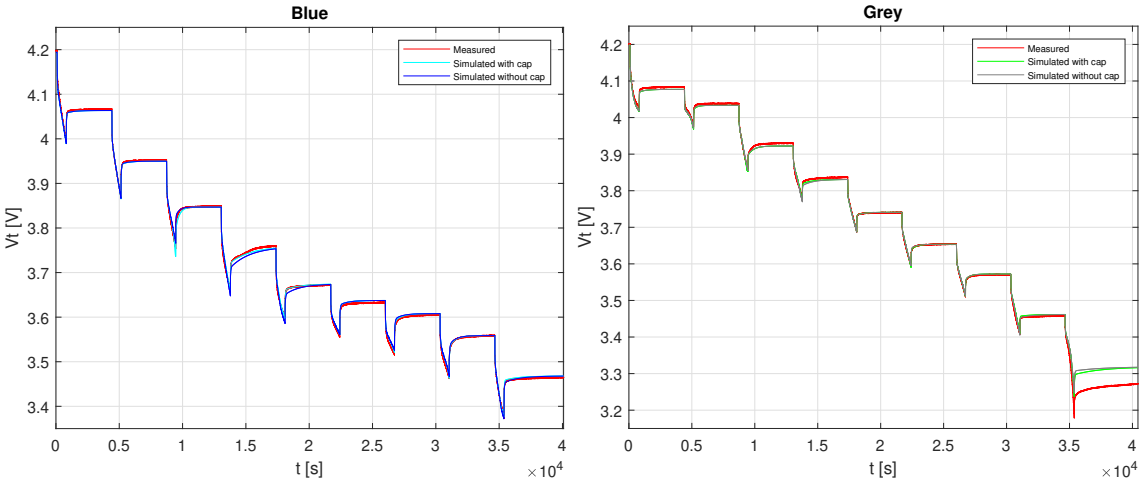

Figure 4.13: ECM with and without capacitance derivative for grey and blue cell at 25°C.

Figure 4.14 shows the RMSE between simulations with and without the capacitive derivative versus the measured data. It can be seen that deviations between the two methods are small and that the overall error is low. The mean error was calculated for the blue cell to be 0.1050% without the derivative term and 0.0727% with the derivative term. This indicates that the accuracy gain of adding the derivative for the blue cell is small. The grey cell modeling performance was analyzed by analyzing the median value due to the large modeling error at the ninth pulse, see Section 4.3 for an explanation. The median value for the grey cell without derivative was 0.1317% and with derivative term 0.1388%. The difference between them is really small and the outcome is not consequent compared to the blue cell since the modeling method without capacitance now performs marginally better.

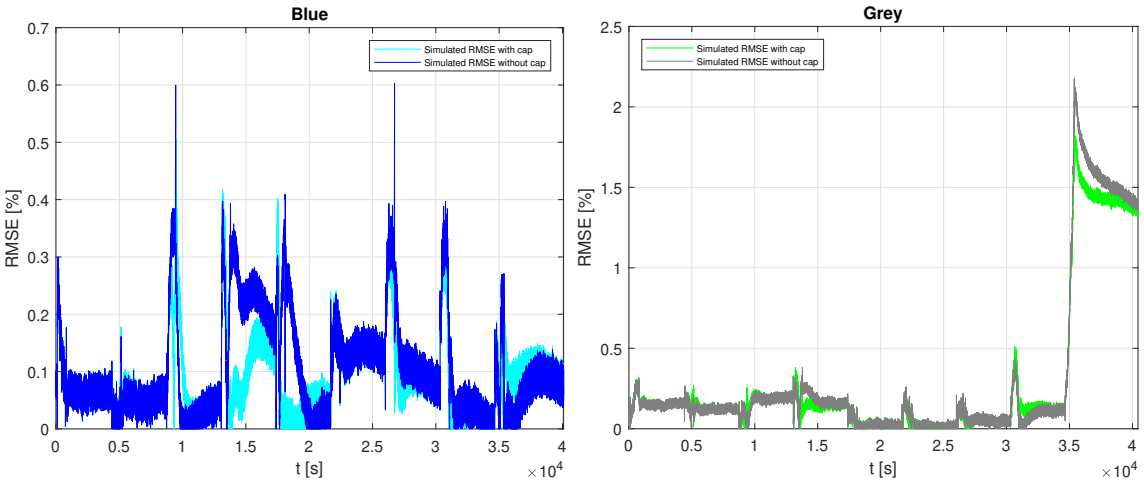

Figure 4.14: RMSE of ECM modeling with and without capacitance derivative for grey and blue cell vs measured output at 25°C.

By investigating (3.3) and (3.4), it can be seen that the capacitive term consists of the following equations: $\frac{\dot{C}_1(t)}{C_1(t)}$ and $\frac{\dot{C}_2(t)}{C_2(t)}$. By combining these fractions with the capacitive values during discharge in Figure 4.15, it can be observed that the fraction value will become small and will not affect the estimated voltages V_1 and V_2. Therefore the ECM will be modeled without the time derivative of the capacitance since the gain in accuracy is close to none, and there is a larger benefit in using a less complex model.

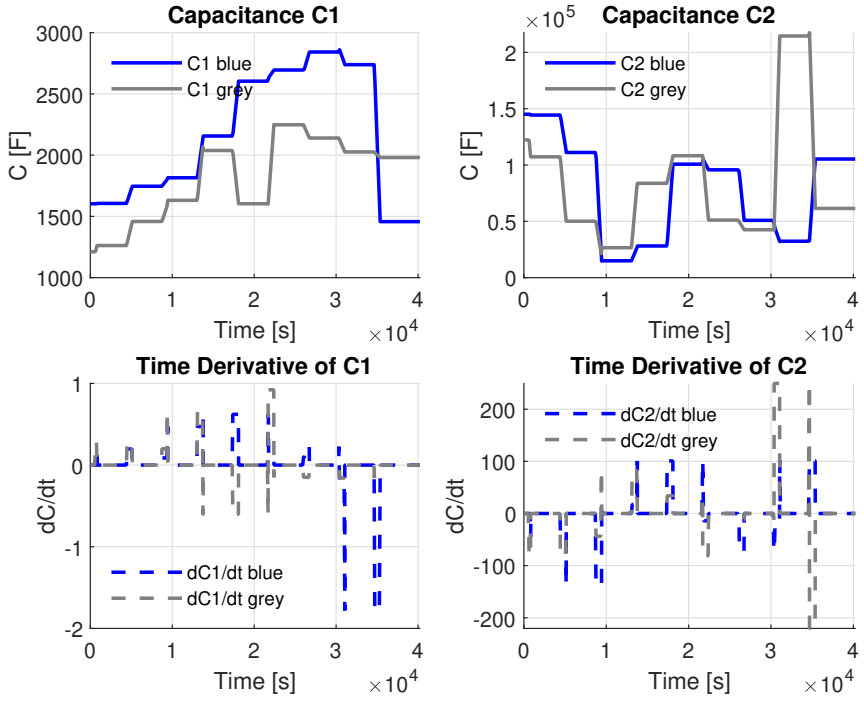

Figure 4.15: Capacitance and capacitance derivative of ECM during the charge for grey and blue cell at 25°C.

4.4 SOC

Three different SOC estimations have been evaluated and tested. These SOC algorithms have been running on the same current profiles as the Keysight. The actual SOC level at each time step can be calculated by using CC (2.7) on the unbiased reference current signal. The initial SOC level was found by combining the measured voltage starting point with the corresponding OCV function for that specific starting temperature.

4.4.1 Coulomb counting

In Figure 4.16 the difference between the actual SOC and CC method is shown. It can be seen that the CC drifts over time, with the error increasing. The drift is due to the integration of measurement noise within the algorithm. The CC algorithm lacks a built in method for correcting itself and therefore needs to be reset over time in order to find the right starting point and remove the drift. This results in

SOC estimation experiencing more drift the longer the batteries are used. The CC algorithm is also dependent on a good initial guess since it is not self correcting. A BMS system can use the OCV when the vehicle is turned off to find a new initial guess for the CC algorithm. However, if the vehicle has only been turned of for a short amount of time (less than an hour), the battery will not be stabilized resulting in an incorrect SOC readout.

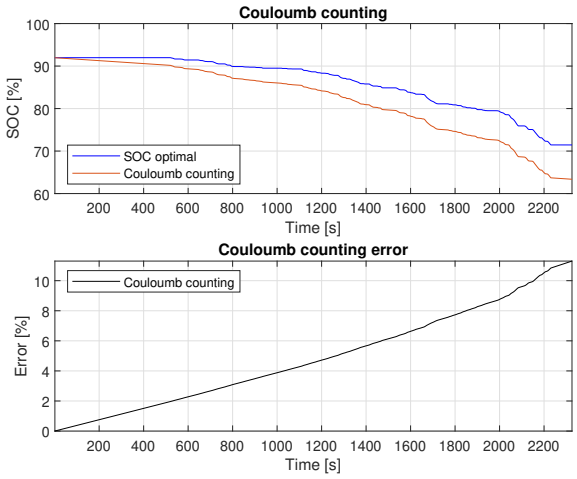

Figure 4.16: CC SOC vs actual SOC on WLTP driving cycle for blue cell.

4.4.2 Kalman filtering discharge pulse

The UKF and EKF estimation of SOC under the discharge pulses and their corresponding errors can be found in Figure 4.17 and 4.18. Both of the filter's initial guess of SOC was set to 50%.

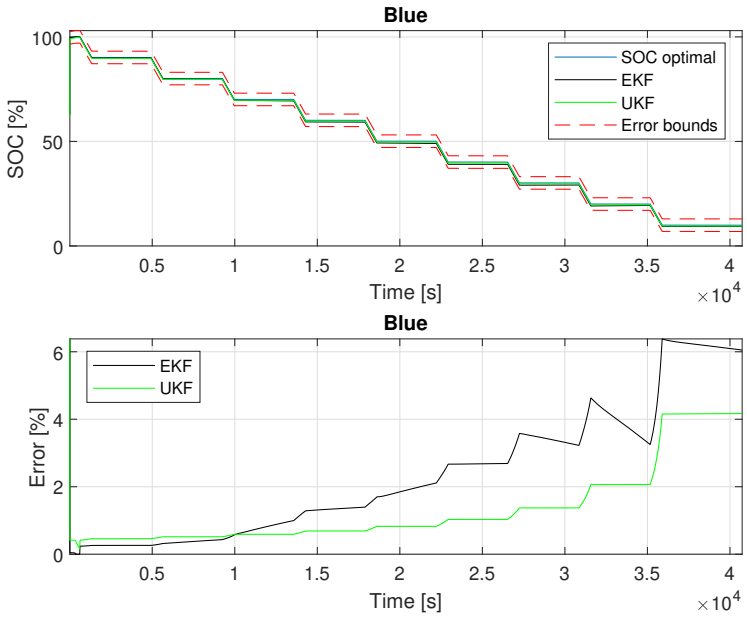

Figure 4.17: EKF and UKF SOC vs actual SOC on discharge pulse current for blue cell.

It can be seen that both the EKF and the UKF perform very well and lies within the +/-3% SOC error bounds. The error between the Kalman filters SOC and actual SOC increases with time. This comes as no surprise since a small estimation error creates a large error in SOC. The EKF max error is around 6.1% when the actual SOC is 10%. This means that the EKF is estimating SOC to be around 10.61%. This is well within the 3% error bounds set as a goal for both of the Kalman filters. By looking at the SOC-OCV curve in Figure 4.2, it can be seen that the voltage dynamics change rapidly with SOC, resulting in a region that is harder to estimate. Hence the error in SOC estimation will increase. It can also be seen that the UKF performs better overall compared to the EKF. This could be due to multiple reasons. The UKF does not perform a linearization but instead utilizes the probability distribution and runs a set of sigma points through the non-linear process and measurement model. This results in a more accurate SOC state estimation since no linearization is done. Another difference lies in the filter tuning. The two Kalman filters are tuned differently and separately resulting in different behaviors. Therefore, the marginally better performance might also be due to better tuning.

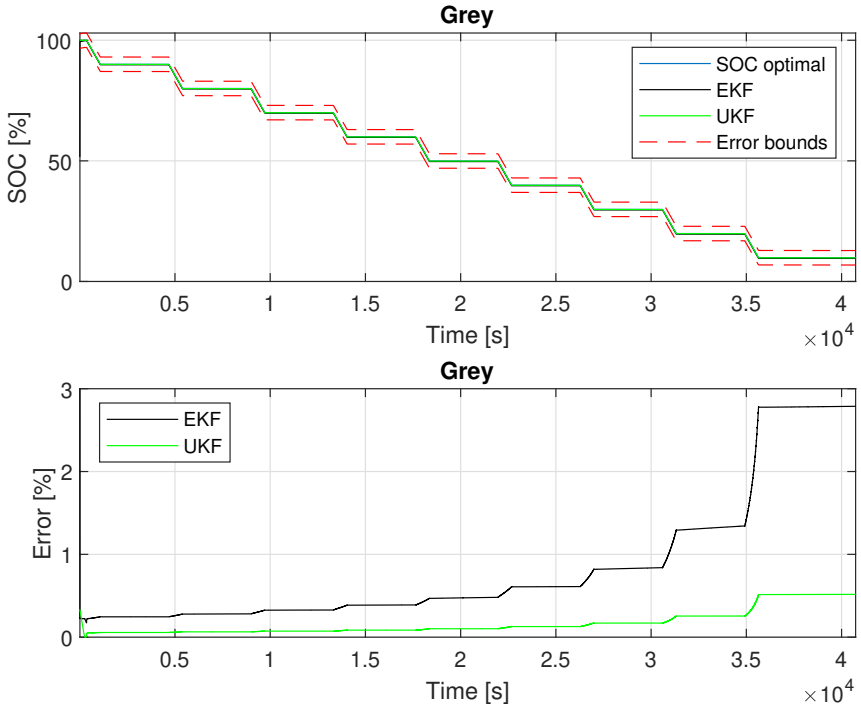

Figure 4.18: EKF and UKF SOC vs actual SOC on discharge pulse current for grey cell.

The same phenomena can be observed for the grey cell. Both the EKF and the UKF perform well, with the UKF performing slightly better. The overall error is lower for the grey cell compared to the blue one. This has to do with that the grey cell model has higher accuracy due to a more repetitively OCV behavior with less measurement and estimation error compared to the blue cell.

4.4.3 Kalman filtering WLTP cycle

To test the robustness of the Kalman filters the WLTP cycles presented in Section 3.8.3 were used. Both of the Kalman filters initial guess of SOC is 50%. The result from the blue cell can be seen in Figure 4.19.

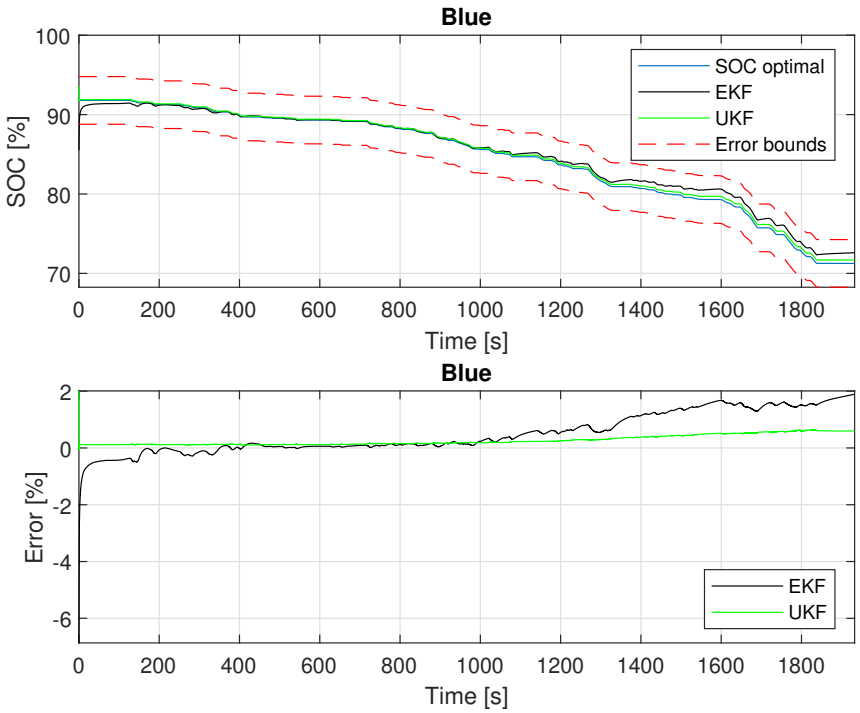

Figure 4.19: EKF and UKF SOC vs actual SOC on WLTP cycle for the blue cell.

It can clearly be seen that both the EKF and UKF perform very well and that despite the initial guess being the worst scenario, both algorithms quickly converge to accurately estimate SOC. Overall, the UKF performs slightly better than the EKF. This is most likely due to the fact that the SOC is within an interval where the OCV curve is highly nonlinear, resulting in better estimation by the UKF which doesn't rely on linearization. In Figure 4.20 the result from the grey cell is presented.

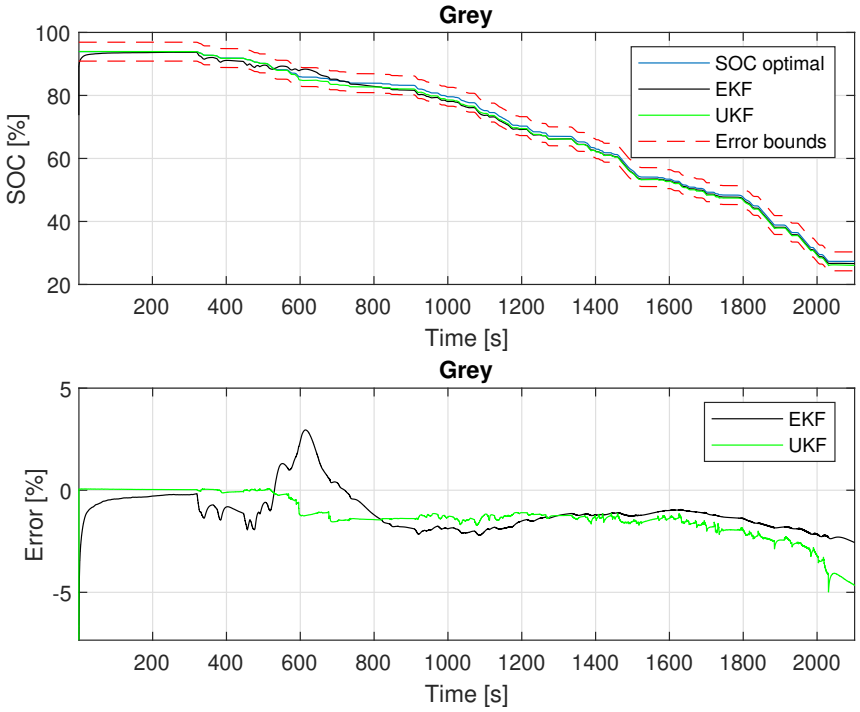

Figure 4.20: EKF and UKF SOC vs actual SOC on WLTP cycle for the grey cell.

Just as for the blue cell it can be seen that both the EKF and the UKF perform very well. In this case, the EKF slightly outperforms the UKF. This is likely due to better tuning of the EKF. Since the UKF has six tuning parameters compared to EKF which only has three, it is more likely to tuning errors. It can also be seen that both UKF and EKF manages to find the right SOC level even though the initial guess is at 50% SOC. If the initial guessing error is excluded it can be seen that the error in SOC is below 4.5% both grey and blue cell.

4.4.4 Kalman filtering robustness

The Kalman filter is a self correcting SOC algorithm, the filter can handle incorrect guesses of initial SOC and still find the right estimated value. In Figure 4.21 the EKF algorithm is represented with six different initial SOC guesses. It can clearly be seen that the algorithm finds the optimal value (OPT) and that a guess close to the actual SOC value corresponds to faster converging. The UKF has the same type of behavior but converges faster towards actual SOC.

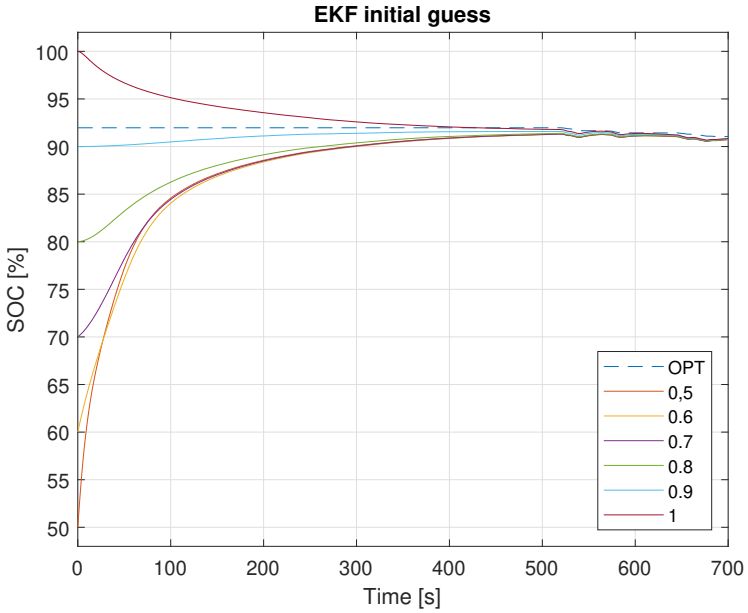

Figure 4.21: EKF SOC estimation with different initial SOC.

4.5 SOH

The linear SOH regression on OCV for the blue and the grey cell can be seen in Figure 4.22, together with the resulting equations (4.1) and (4.2).

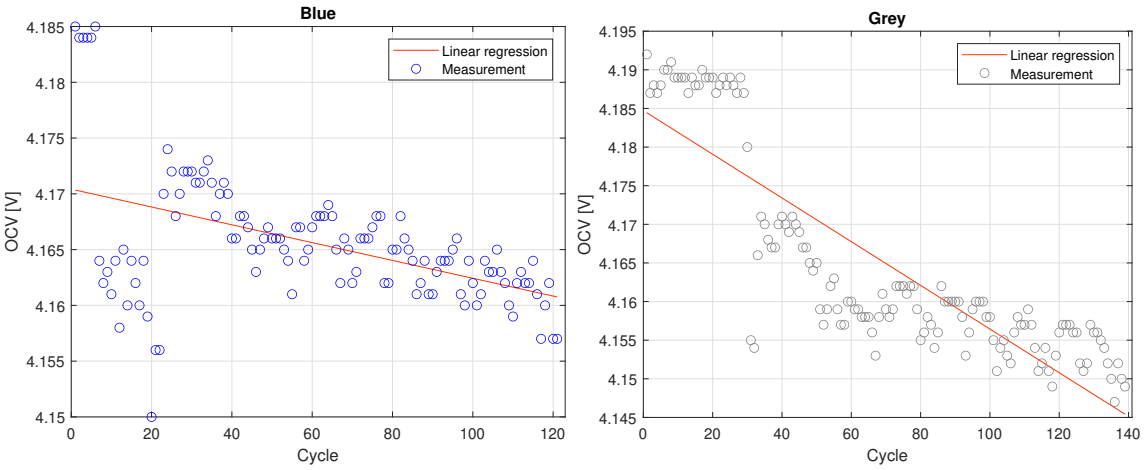

Figure 4.22: Linear regression of OCV for the blue and the grey cell.

$$SOH_{blue,OCV} = 4.1704 - 7.9881 \times 10^{-5} \times n_{cycles} \tag{4.1}$$

$$SOH_{grey,OCV} = 4.1847 - 2.8285 \times 10^{-4} \times n_{cycles} \tag{4.2}$$

Where n_{cycles} is the number of cycles. It can be seen that the degradation is about 3.5% faster for the grey cell. The spread of the OCV is fairly good for both cells. Some outliers can be seen for the first 20 cycles for both the blue and the grey cell.

This could be due to the cell still breaking in. In Figure 4.23 the linear regression of the capacity can be seen, with the resulting equations (4.3) and (4.4).

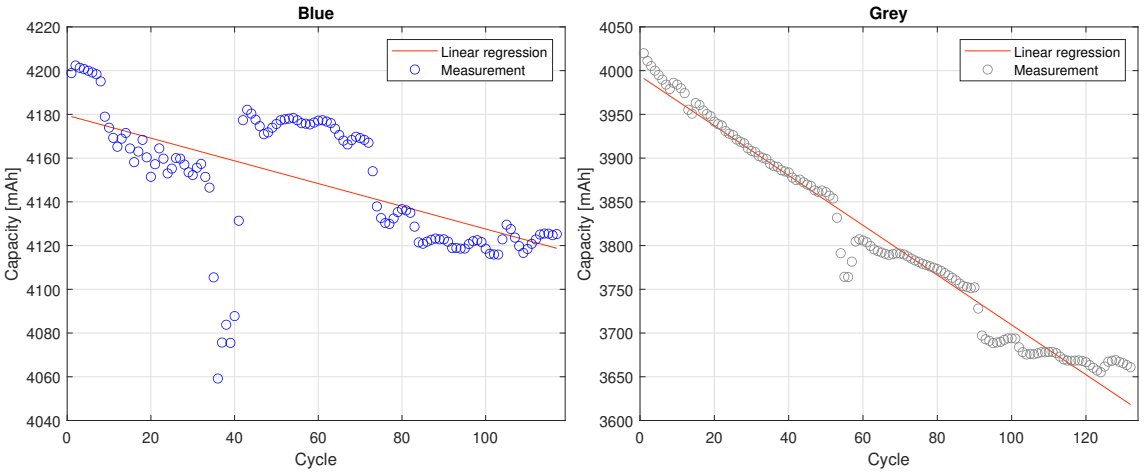

Figure 4.23: Linear regression of capacity for the blue and the grey cell.

$$SOH_{blue,C} = 4179.5 - 0.5195 \times n_{cycles} \tag{4.3}$$

$$SOH_{grey,C} = 3993.9 - 2.8464 \times n_{cycles} \tag{4.4}$$

The capacity degrades about 550% faster for the grey cell compared to the blue, which is a big difference compared to the OCV result. It can also be seen that even if the blue cell is rated at 4Ah, the cells initial capacity is around 4.2Ah, whereas the grey cell is around 4.03Ah. Final SOH for both cells and both methods can be seen in the list below.

- $SOH_{blueOCV} = 98.97\%$
- $SOH_{blueC} = 98.09\%$
- $SOH_{greyOCV} = 98.71\%$
- $SOH_{greyC} = 90.59\%$

For the blue cell, both methods produce similar results, with the capacity method being slightly more conservative. For the grey cell this remains true but the methods don't produce similar results. The difference between the methods is 8.12%. Which method to use for a BMS depends on what parameter is more important for the application. The result could also be combined to give an averaged SOH, including other factors that could impact the SOH such as temperature.

4.6 SOP

In Figure 4.24 the result of the algorithm described in Section 3.6 for the blue cell is presented.

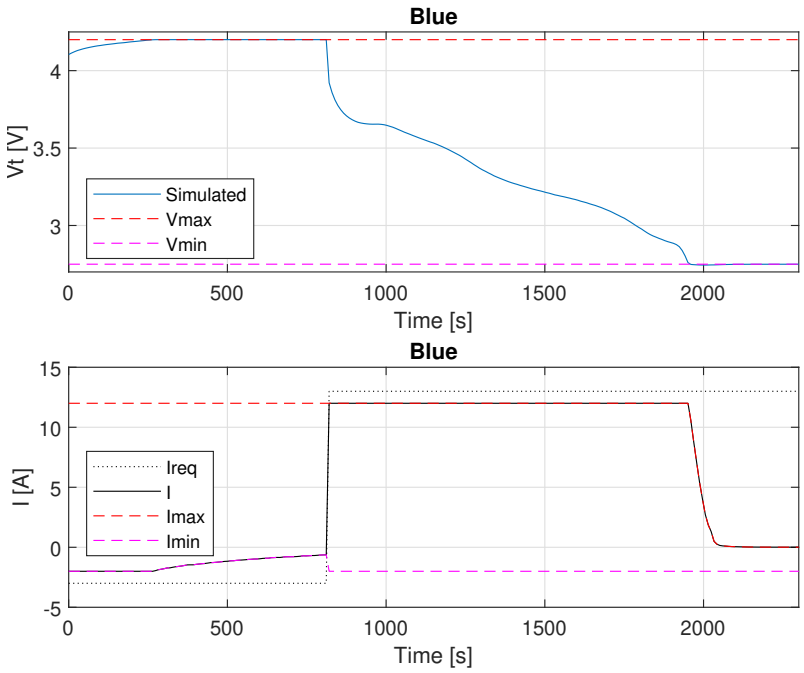

Figure 4.24: SOP algorithm regulating the current to keep the voltage inside permitted range for the blue cell.

It can be seen that the algorithm efficiently regulates the permitted current for both discharge and charge. For the charging case, the maximum allowed voltage of 4.2V is met and not exceeded. It can be seen that the requested charge current is at -3A, but since the blue cell only is rated for -2A while charging the algorithm regulates that. When the max voltage is achieved, the algorithm slowly reduces the allowed current in order to not exceed the allowed max voltage. The same can be seen for the discharge case. Firstly the current is limited by the rated discharge current, which is 12A for the blue cell. When the minimum allowed voltage is achieved, the current is reduced. In Figure 4.25 the same phenomena can be seen for the grey cell.

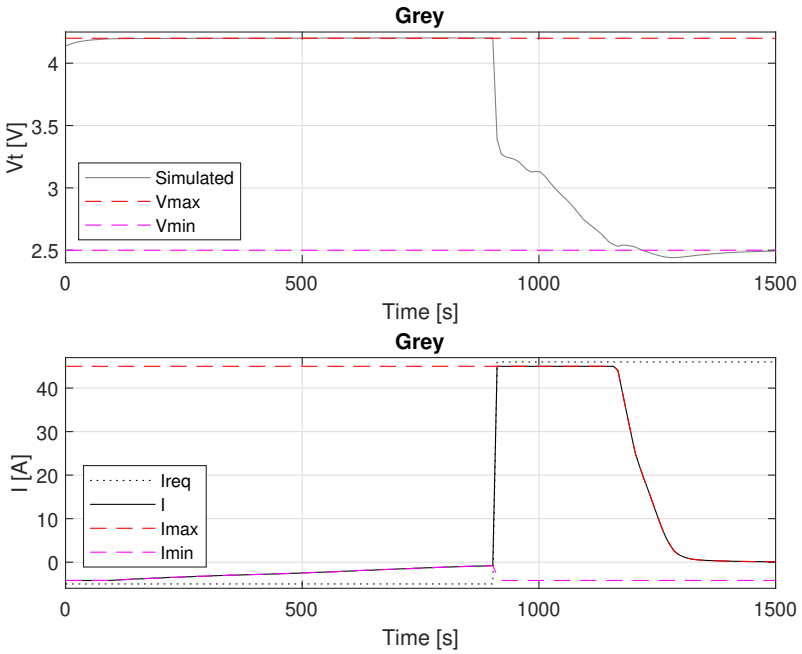

Figure 4.25: SOP algorithm regulating the current to keep the voltage inside permitted range for the grey cell.

For the grey cell, the maximum allowed charge current is -4.2A and the max allowed discharge current is 45A. Just as for the blue cell, it can be seen that the algorithm successfully regulates the voltage of the grey cell to keep it close to its allowed voltage range. Something to notice for the grey cell however, is that the voltage goes under the allowed minimum voltage for a short time. This is likely due to the fact that our model runs with dynamic parameters, which makes it hard for the algorithm to predict the voltage drop as R_0 changes. In Figure 4.26 the results of the predictive power algorithm described in Section 3.6.1 are presented. Both the simulations start at 50% SOC.

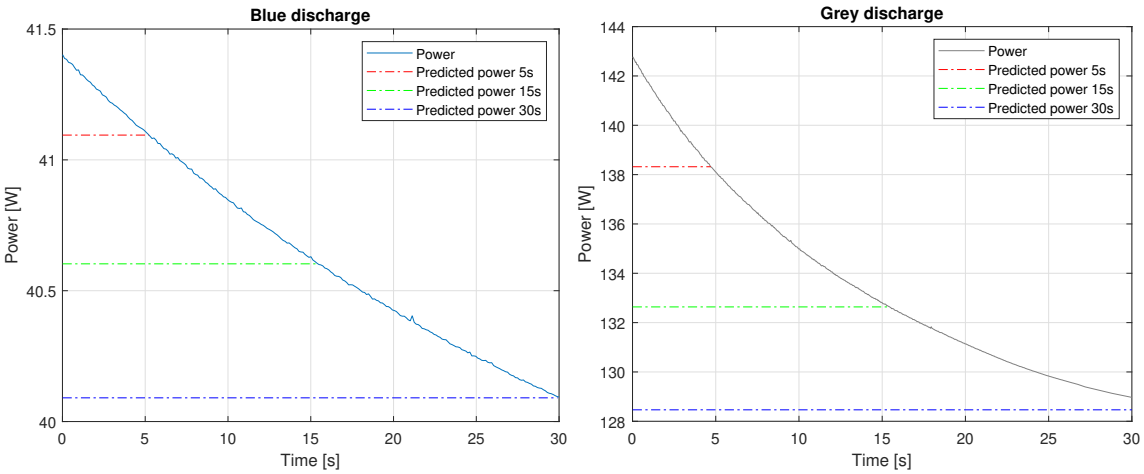

Figure 4.26: Predicted power 5s, 15s and 30s compared to actual power available for the blue and the grey cell.

It can be concluded that the algorithm predicts the available power rather well, considering that the algorithm can't predict the parameters of the model changing. It can be seen that the predicted power for all three time periods matches very well for the blue cell. It can be seen that this also remains true for the grey cell. For the 5s and 15s predicted power, a small deviation from the actual power can be seen. However, since the available power is around three times that of the blue, the percentage error remains small.

4.7 Thermal modeling

In Figure 4.27, a comparison between measured and simulated temperatures is presented for the blue and grey cells. Discharge pulses were conducted for the blue cell at an ambient temperature of 15°C, while charge pulses were performed for the grey cell at an ambient temperature of 10°C.

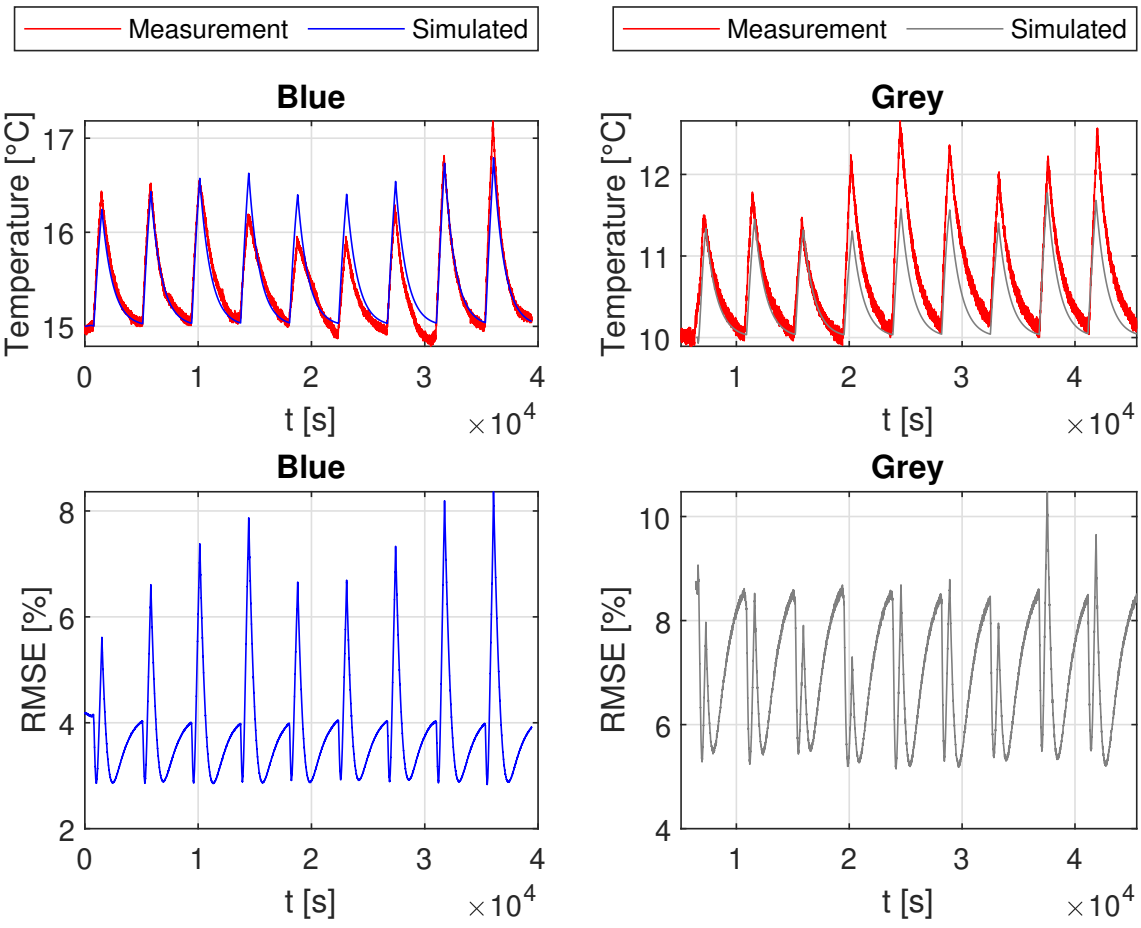

Figure 4.27: Measured surface temperature of the blue and grey cell with simulated surface temperature for different ambient temperatures. The error between measured and simulated is also presented.

The results show that the thermal model performs quite well, with a mean error of 3.86% for the blue cell and 7% for the grey. The difference in magnitude of the

mean error could be due to better estimated values of the heat transfer coefficient and specific heat capacity. Since the temperature measurement and the current pulses were not synchronized in time, a small contribution to the error could be due to the simulated and measured not aligning in time.

4.7.1 ECM combined with thermal model

The results from the thermal model performance on the WLTP cycle for the blue and grey cells are presented in Figures 4.28 and 4.29.

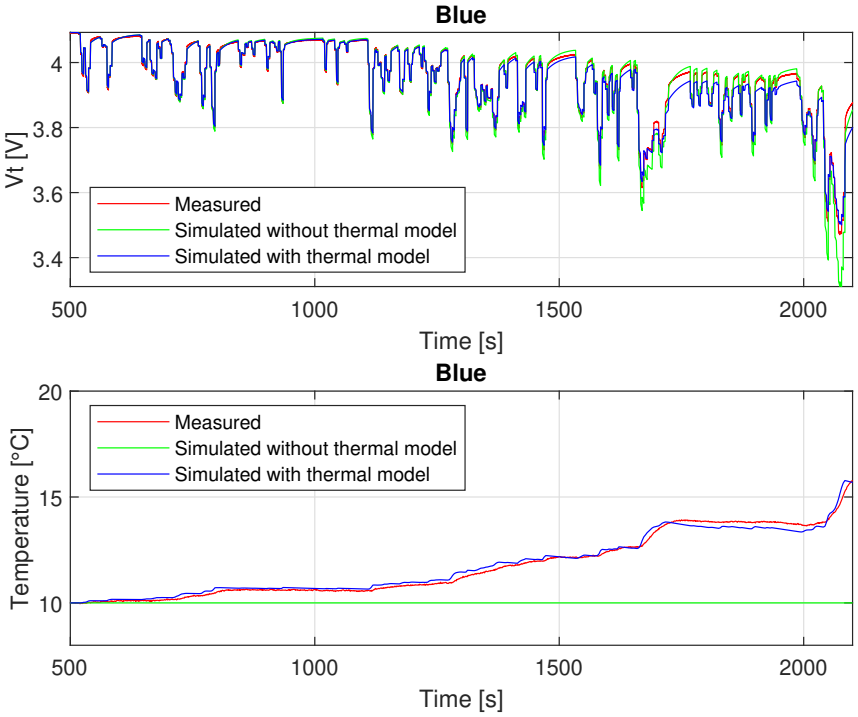

Figure 4.28: Measured terminal voltage and surface temperature of the grey cell together with simulated.

It can be seen that the thermal model accurately predicts the measured temperature, and that the models performance increases as a result of it. The model without the thermal model tends to overestimate the resistive drops a lot more. It is worth mentioning that the blue cell's temperature only increased with about 5°C, which means that the thermal model only interpolates between 10°C and 15°C.

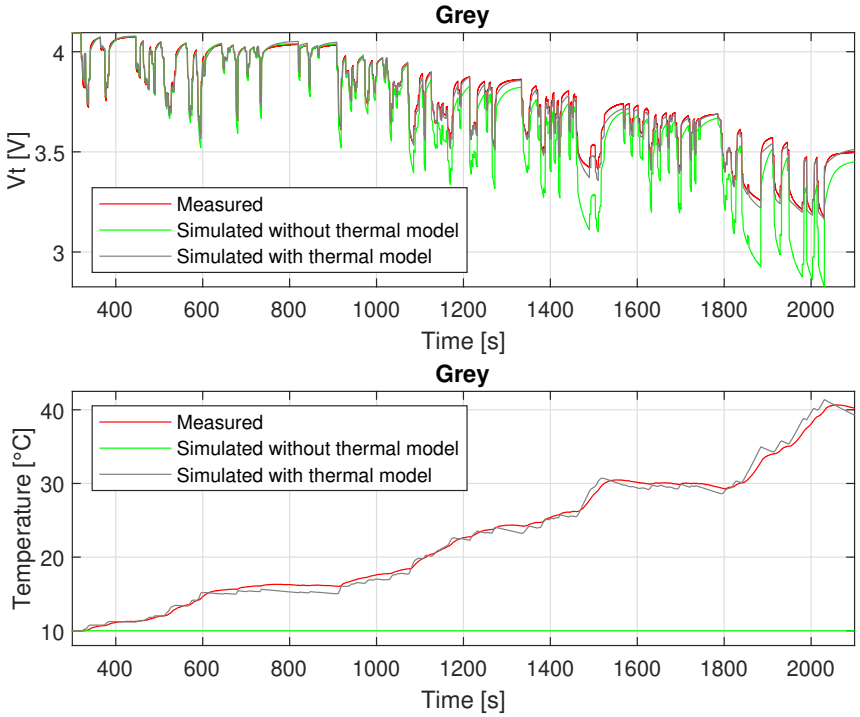

Figure 4.29: Measured terminal voltage and surface temperature of the grey cell together with simulated.

For the grey cell, a larger increase in performance can be seen. This is due to that the cell's temperature increased to around 40°C, which meant that the parameters from 10°C will be a poor representation of the cell at 40°C. This shows the importance of both a thermal model, but also the temperature dependence of a lithium ion battery.

5
Conclusion

5.1 Battery model conclusion

In the sections below the conclusion for the thesis connected to the first objective is presented together with the project aim. The methods used for ECM, parameterization and measurements lay a solid foundation for a good performing battery model, and fulfills the project aim concerning the battery modeling and parameterization.

5.1.1 ECM modeling

It can be concluded that the dual RC-link ECM without capacitive derivative is sufficient enough in order to capture the behavior of the lithium ion battery cells chosen for this project. By only modeling two RC-links without capacitive derivative the complexity of the system is reduced, resulting in a model that is less computationally demanding to run on an ECU. It can be concluded that the mean modeling error for the blue cell is 0.1050% while median error for the grey cell is 0.1317%. By analyzing the results it can also be concluded that the model is capable of capturing both charge and discharge characteristics with high precision. The decision to implement the ECM as a state-space representation makes the model modular and beneficial, as it allows for the same state equations to be used in Kalman filtering, thereby improving time efficiency since multiple models do not need to be used. This method improves modeling efficiency by reducing the modifications needed in Simulink for both ECM and Kalman filtering.

5.1.2 ECM measurement and parameterization approach

The parameterization and measurement method is accurate and good enough to provide valuable and useful output data. It can be concluded that the chosen C-rate for the OCV measurement was good since the OCV output has been kept close to the actual without increasing the measurement time. The conclusion regarding temperature resolution for OCV is that the blue cell needed the 5°C resolution due to the large difference between the highest and lowest temperature while the grey cell could have been parameterized with larger temperature spans and still provided an accurate output. The measurement time for OCV will be reduced by 40h for every temperature that does not need to be measured. It can be concluded that the parameterization and measurement method used for the resistive and capacitive components provides good values for the model. Since the measured and model output for grey and blue only differs with less than 2.25% for the worst case where

the grey cell has been parameterized with to short relaxation time on ninth pulse. The final conclusion is that the grey discharge measurement needs longer relaxation time than what has been used, for the last pulse in order for the cell chemistry to stabilize and reach up to the right OCV value.

5.1.3 Battery thermal modeling

Based on the results, it can be concluded that the model performs adequately considering the very simple approach of only modeling the voltage difference from OCV and terminal voltage as a thermal loss. Despite the model's limited accuracy, evidenced by an RMSE of 3.86% for the blue cell and 7% for the grey, it notably enhances the battery model's performance under prolonged and demanding current cycles. This improvement is particularly evident when the cell temperature surpasses the ambient temperature. This improvement was evident in Section 4.7.1 for both cells, where the thermal model enabled to accurately interpolate between values as the temperature increased.

5.2 BMS conclusion

In conclusion, the methodologies employed in this thesis lay a solid foundation for a BMS. Through the measurement campaign, parameters could be effectively identified in a time efficient manner. These parameters were then implemented into the model, which then was integrated into various systems including the EKF, UKF, SOP and SOH algorithms. The integration of these systems forms the basis of an exceptional BMS capable of predicting future power availability, estimating SOC, terminal voltage, the temperature of the battery, and lastly the aging of the cell. This integration fulfills the project aim with respect to SOC, SOH and SOP.

5.2.1 SOC conclusion

It can be concluded that both the EKF and UKF present viable options for estimating SOC for a BMS application. While the UKF generally outperforms the EKF due to its nonreliance on linearization, it is often more challenging to fine tune. However, the performance discrepancy between the EKF and UKF is marginal where both filters performs within the 3% SOC error bounds. This implies that for a vehicle application are their performance satisfactory since the difference between optimal and estimated SOC and is below 4.5% error for the used WLTP cycle. Additionally, it can be concluded that the CC method remains viable under the condition that a very precise current sensor is used in the application. Otherwise, the CC method will drift away from the actual SOC due to measurement noise, and the estimation technique will perform poorly.

5.2.2 SOH conclusion

The methods employed in this thesis appear to effectively capture the aging effect of both batteries. The decline in both OCV and capacity is clearly evident in the

measurement data, and the rate of decline can be observed in the resulting linear regression equations. Depending on the application, either the OCV method or the capacity method may be preferred. For instance, if an application relies on the batteries for low power, long duration operation, the capacity method would be preferred. Alternatively, a weighted SOH estimation could utilize both methods. During testing, it was found that the blue cell, which was rated at 4Ah, actually had a capacity closer to 4.2Ah. After cycling, the cell's capacity remained around 4.12Ah, still exceeding its nominal capacity value. The grey cell's start capacity was in fact 4Ah, and after approximately 140 cycles only managed to retain around 3.65Ah. This indicates that the grey cell ages much faster than the blue cell. It can be concluded that the blue cell's actual factory capacity is likely closer to 4.2Ah. However, to confirm this, more measurements from additional cells would be necessary to capture the spread across cells.

5.2.3 SOP conclusion

Another conclusion drawn from this analysis is that the implemented algorithms accurately determine the SOP for both cells. The algorithms effectively restrict the current to prevent it from surpassing the cells rated discharge and charge currents. Moreover, they ensure that the current does not exceed the maximum voltage or fall below the minimum voltage within an acceptable tolerance. Upon reviewing the results, it was observed that the algorithm slightly overestimated the allowable current during discharge, resulting in the voltage momentarily dropping below the permitted minimum voltage. However, since this occurrence was brief and very close to the minimum voltage, it is unlikely to cause harm to the cell. Regarding the power prediction algorithms, it could also be concluded that they successfully predict the power levels for 5s, 15, and 30s into the future. This held true for both the blue and the grey cells, and the small estimation error is likely negligible in a real application.

5.3 Suggestions for future work

Several topics are of interest for further exploration of potential performance benefits for the BMS model. It was evident from the results that the last discharge pulse for the grey cell did not have enough time to reach its OCV value. Therefore, investigating whether the model would perform better with parameters extracted from the ninth pulse with a longer relaxation time, allowing it to reach a more realistic OCV value in the U4-U5 segment, would be interesting. Another aspect to evaluate the BMS performance would be to scale up the model from a single battery cell to a battery pack. Testing the models and algorithms in this configuration would assess their performance for a battery pack. In conjunction with this, it would be interesting to enhance the thermal model by incorporating a coolant system for the entire battery pack. This enhancement would enable simulation of how an eventual coolant system would be dimensioned and where eventual hot spots in the battery pack would appear. Finally, it would be of interest to enhance the battery model by incorporating a hysteresis component, investigating whether the model's

performance and if it can be implemented in an time effective manner.

Bibliography

[1] European Parliament, "Co2 emissions from cars: Facts and figures," *European Parliament*, 2019, Accessed: 06 February 2024. [Online]. Available: https://www.europarl.europa.eu/news/en/headlines/society/20190313STO31218/co2-emissions-from-cars-facts-and-figures-infographics.

[2] Alternative Fuels Data Center, "Alternative fuels data center: Electric vehicle benefits and considerations," *Alternative Fuels Data Center*, 2024, Accessed: 06 February 2024. [Online]. Available: https://afdc.energy.gov/fuels/electricity_benefits.html.

[3] X. Gong, R. Xiong, and C. C. Mi, "Study of the characteristics of battery packs in electric vehicles with parallel-connected lithium-ion battery cells," *2014 IEEE Applied Power Electronics Conference and Exposition - APEC 2014*, pp. 3218–3224, 2014. DOI: 10.1109/APEC.2014.6803766.

[4] Y. Lu *et al.*, "A method of cell-to-cell variation evaluation for battery packs in electric vehicles with charging cloud data," *eTransportation*, vol. 6, p. 100 077, 2020. DOI: 10.1016/j.etran.2020.100077. [Online]. Available: https://www.sciencedirect.com/science/article/pii/S2590116820300345.

[5] H. Rahimi-Eichi, U. Ojha, F. Baronti, and M.-Y. Chow, "Battery management system: An overview of its application in the smart grid and electric vehicles," *IEEE Industrial Electronics Magazine*, vol. 7, no. 2, pp. 4–16, 2013. DOI: 10.1109/MIE.2013.2250351.

[6] W. Zhou, Y. Zheng, Z. Pan, and Q. Lu, "Review on the battery model and soc estimation method," *Processes*, vol. 9, no. 9, p. 1685, 2021, ISSN: 2227-9717. DOI: 10.3390/pr9091685. [Online]. Available: https://www.mdpi.com/2227-9717/9/9/1685.

[7] H. Huang, C. Bian, M. Wu, D. An, and S. Yang, "A novel integrated SOC–SOH estimation framework for whole-life-cycle lithium-ion batteries," *Energy*, vol. 288, p. 129 801, 2024, ISSN: 0360-5442. DOI: 10.1016/j.energy.2023.129801. [Online]. Available: https://www.sciencedirect.com/science/article/pii/S036054422303195X.

[8] L. Mauler, F. Duffner, W. Zeier, and J. Leker, "Battery cost forecasting: A review of methods and results with an outlook to 2050," *Energy & Environmental Science*, vol. 14, 2021. DOI: 10.1039/D1EE01530C.

[9] L. Zhang, T. Ji, S. Yu, and G. Liu, "Accurate prediction approach of soh for lithium-ion batteries based on lstm method," *Batteries*, vol. 9, no. 3, p. 177, 2023. DOI: 10.3390/batteries9030177. [Online]. Available: https://www.mdpi.com/2313-0105/9/3/177.

[10] C. E. L. Foss, "Thermal stability and electrochemical performance of graphite anodes in li-ion batteries," Doctoral theses at NTNU, 2014:101. IMT-Report 2014:201. ISBN 978-82-326-0126-4 (printed ver.), ISBN 978-82-326-0127-1 (electronic ver.), ISSN 1503-8181. © Carl Erik Lie Foss. See discussions, stats, and author profiles for this publication at: https://www.researchgate.net/publication/323446422, Thesis for the degree of Philosophiae Doctor, Norwegian University of Science et al., Apr. 2014.

[11] A. N. Laboratory, *Nanoscale research: Big impact*, Accessed: 2024-05-15, 2010. [Online]. Available: https://www.flickr.com/photos/argonne/5029455937.

[12] A. Narayan, "State and parametric estimation of li-ion batteries in electrified vehicles," Ph.D. dissertation, KTH Royal Institute of Technology, Stockholm, 2017. [Online]. Available: https://www.diva-portal.org/smash/get/diva2:1154001/FULLTEXT01.pdf.

[13] B. Sundén, *Details*. Academic Press, 2019, ch. 6, p. 95, ISBN: 978-0-12-816950-6. DOI: 10.1016/C2018-0-01247-5.

[14] H. Perez, J. Siegel, X. Lin, A. Stefanopoulou, Y. Ding, and M. Castanier, "Parameterization and validation of an integrated electro-thermal cylindrical LFP battery model," *Journal of Dynamic Systems, Measurement, and Control*, vol. 3, 2012. DOI: 10.1115/DSCC2012-MOVIC2012-8782.

[15] F. Barbir, *PEM fuel cells: theory and practice*. Academic press, 2012.

[16] G. Larrat, "Open-circuit-voltage hysteresis measurement and modelling of LiFePO4 batteries," TRITA-ITM-EX 2023:489, M.S. thesis, KTH Royal Institute of Technology, Gothenburg, Sweden, 2023.

[17] B. Sundén, *Details*. Academic Press, 2019, ch. 6, p. 94, ISBN: 978-0-12-816950-6. DOI: 10.1016/C2018-0-01247-5.

[18] M. Wu, L. Qin, and G. Wu, "State of power estimation of power lithium-ion battery based on an equivalent circuit model," *Journal of Energy Storage*, vol. 51, pp. 1–9, 2022, ISSN: 2352-152X. DOI: 10.1016/j.est.2022.104538. [Online]. Available: https://www.sciencedirect.com/science/article/pii/S2352152X22005564.

[19] EPIC Power, *An028: Soc, soh, sop definitions*, https://epicpower.es/wp-content/uploads/2020/08/AN028_SoC-SoH-SoP-definitions_v3.pdf, 2020.

[20] X. Hu, S. Li, and H. Peng, "A comparative study of equivalent circuit models for li-ion batteries," *Journal of Power Sources*, vol. 198, pp. 359–367, Jan. 2012. DOI: 10.1016/j.jpowsour.2011.10.013.

[21] A. Melcher, C. Ziebert, M. Rohde, B. Lei, and H. J. Seifert, "Ecm models for li-ion batteries – a short mathematical survey and simulations," *Jahrestagung KIT-Zentrum Energie*, 2016.

[22] S. Li, J. Li, and H. Wang, "Big data driven lithium-ion battery modeling method: A cyber-physical system approach," in *2019 IEEE International Conference on Industrial Cyber Physical Systems (ICPS)*, Taipei, Taiwan, 2019, pp. 161–166. DOI: 10.1109/ICPHYS.2019.8780152.

[23] G. Plett, *Battery Management Systems, Volume I: Battery Modeling*. Artech, 2015.

[24] M. Gaberšček, "Impedance spectroscopy of battery cells: Theory versus experiment," *Current Opinion in Electrochemistry*, vol. 32, p. 100 917, 2022, ISSN: 2451-9103. DOI: https://doi.org/10.1016/j.coelec.2021.100917. [Online]. Available: https://www.sciencedirect.com/science/article/pii/S2451910321002313.

[25] H. Watanabe, S. Omoto, Y. Hoshi, I. Shitanda, and M. Itagaki, "Electrochemical impedance analysis on positive electrode in lithium-ion battery with galvanostatic control," *Journal of Power Sources*, vol. 507, p. 230 258, 2021, ISSN: 0378-7753. DOI: https://doi.org/10.1016/j.jpowsour.2021.230258. [Online]. Available: https://www.sciencedirect.com/science/article/pii/S0378775321007771.

[26] L. A. Middlemiss, A. J. Rennie, R. Sayers, and A. R. West, "Characterisation of batteries by electrochemical impedance spectroscopy," *Energy Reports*, vol. 6, pp. 232–241, 2020, 4th Annual CDT Conference in Energy Storage Its Applications, ISSN: 2352-4847. DOI: https://doi.org/10.1016/j.egyr.2020.03.029. [Online]. Available: https://www.sciencedirect.com/science/article/pii/S2352484720303103.

[27] E. Arksand, *Parametrization of a lithium-ion battery*, 2021.

[28] B. Xia, R. Huang, Z. Lao, *et al.*, "Online parameter identification of lithium-ion batteries using a novel multiple forgetting factor recursive least square algorithm," *Energies*, p. 19, 2018. DOI: 10.3390/en11113180. [Online]. Available: https://doi.org/10.3390/en11113180.

[29] Y. Wu, H. Chen, L. Cao, J. Duan, X. Chen, and J. Zhai, "Research on online identification of lithium-ion battery equivalent circuit model parameters," in *2022 9th International Forum on Electrical Engineering and Automation (IFEEA)*, 2022, pp. 130–136. DOI: 10.1109/IFEEA57288.2022.10038123.

[30] J. P. Rivera-Barrera, N. Muñoz-Galeano, and H. O. Sarmiento-Maldonado, "Soc estimation for lithium-ion batteries: Review and future challenges," *Electronics*, p. 25, 2017. DOI: 10.3390/electronics6040102.

[31] R. A. Cottis, "Electrochemical noise for corrosion monitoring," pp. 86–110, 2008. DOI: 10.1533/9781845694050.1.86. [Online]. Available: https://www.sciencedirect.com/science/article/pii/B9781845691875500042.

[32] M. Danko, J. Adamec, M. Taraba, and P. Drgona, "Overview of batteries state of charge estimation methods," *Transportation Research Procedia*, vol. 40, pp. 186–192, 2019, ISSN: 2352-1465. DOI: 10.1016/j.trpro.2019.07.029. [Online]. Available: https://www.sciencedirect.com/science/article/pii/S2352146519301905.

[33] L. Zhi, Z. Peng, W. Zhifu, S. Qiang, and R. Yinan, "State of charge estimation for li-ion battery based on extended kalman filter," *Energy Procedia*, vol. 105, pp. 3515–3520, 2017, 8th International Conference on Applied Energy, ICAE2016, 8-11 October 2016, Beijing, China, ISSN: 1876-6102. DOI: https://doi.org/10.1016/j.egypro.2017.03.806. [Online]. Available: https://www.sciencedirect.com/science/article/pii/S1876610217308810.

[34] MathWorks, *Extended and unscented kalman filter algorithms for online state estimation*, https://se.mathworks.com/help/control/ug/extended-and-unscented-kalman-filter-algorithms-for-online-state-estimation.html, Accessed: 2024-03-28.

[35] P. Reshma and V. Joshi Manohar, "Collaborative evaluation of soc, sop and soh of lithium-ion battery in an electric bus through improved remora optimization algorithm and dual adaptive kalman filtering algorithm," *Journal of Energy Storage*, vol. 68, p. 107 573, 2023. DOI: 10.1016/j.est.2023.107573. [Online]. Available: https://doi.org/10.1016/j.est.2023.107573.

[36] S. S. Siwal, G. Nuroldayeva, Y. Serik, D. Adair, B. Uzakbaiuly, and Z. Bakenov, "State of health estimation methods for lithium-ion batteries," *International Journal of Energy Research*, vol. 2023, p. 4 297 545, Mar. 3, 2023, ISSN: 0363-907X. DOI: 10.1155/2023/4297545. [Online]. Available: https://doi.org/10.1155/2023/4297545.

[37] X. Kong, A. Bonakdarpour, B. T. Wetton, D. P. Wilkinson, and B. Gopaluni, "State of health estimation for lithium-ion batteries," *IFAC-PapersOnLine*, vol. 51, no. 18, pp. 667–671, 2018, 10th IFAC Symposium on Advanced Control of Chemical Processes ADCHEM 2018, ISSN: 2405-8963. DOI: https://doi.org/10.1016/j.ifacol.2018.09.347. [Online]. Available: https://www.sciencedirect.com/science/article/pii/S2405896318320329.

[38] C. Liu, M. Hu, G. Jin, Y. Xu, and J. Zhai, "State of power estimation of lithium-ion battery based on fractional-order equivalent circuit model," *Journal of Energy Storage*, vol. 41, p. 102 954, 2021, ISSN: 2352-152X. DOI: https://doi.org/10.1016/j.est.2021.102954. [Online]. Available: https://www.sciencedirect.com/science/article/pii/S2352152X21006691.

[39] S. Zhao, S. Duncan, and D. Howey, "Observability analysis and state estimation of lithium-ion batteries in the presence of sensor biases," *IEEE Transactions on Control Systems Technology*, vol. 25, Oct. 2015. DOI: 10.1109/TCST.2016.2542115.

[40] T. Wik, B. Fridholm, and H. Kuusisto, "Implementation and robustness of an analytically based battery state of power," *Journal of Power Sources*, vol. 287, pp. 448–457, 2015, ISSN: 0378-7753. DOI: 10.1016/j.jpowsour.2015.03.165.

[41] F. Zhu, H. Yan, L. Liu, and X. Liu, "Simulation of thermal behavior of a lithium-ion battery," in *Proceedings of the 2016 5th International Conference on Sustainable Energy and Environment Engineering (ICSEEE 2016)*, Atlantis Press, 2016/12, pp. 528–532, ISBN: 978-94-6252-278-7. DOI: 10.2991/icseee-16.2016.96. [Online]. Available: https://doi.org/10.2991/icseee-16.2016.96.

[42] J. He, R. Youssef, M. S. Hosen, M. Akbarzadeh, J. Van Mierlo, and M. Berecibar, "A novel methodology to determine the specific heat capacity of lithium-ion batteries," *Journal of Power Sources*, vol. 520, p. 230 869, 2022, ISSN: 0378-7753. DOI: https://doi.org/10.1016/j.jpowsour.2021.230869. [Online]. Available: https://www.sciencedirect.com/science/article/pii/S0378775321013549.

[43] R. Xu, "Lithium-ion battery modeling and soc estimation," *Master's Thesis, KTH Royal Institute of Technology*, pp. 1–30, Jun. 2023, ISSN: 1234-5678. DOI: 10.1234/thesis.xu2023.

[44] S. Kocsis Szürke, A. Dineva, and B. Csomós, *Complex testing procedure for 18650 batteries*, 2021. DOI: 10.21227/gg24-sj16. [Online]. Available: https://dx.doi.org/10.21227/gg24-sj16.

DEPARTMENT OF SOME SUBJECT OR TECHNOLOGY
CHALMERS UNIVERSITY OF TECHNOLOGY
Gothenburg, Sweden
www.chalmers.se

CHALMERS
UNIVERSITY OF TECHNOLOGY